

Copyright
by
Isaac Chavez
2010

The Thesis committee for Isaac Chavez

Certifies that this is the approved version of the following thesis

**Magnetic Control of Supersonic Beams: Magnetic Slowing
to Isotope Separation**

APPROVED BY

SUPERVISING COMMITTEE:

Mark G. Raizen, Supervisor

George T. Shubeita

**Magnetic Control of Supersonic Beams: Magnetic Slowing
to Isotope Separation**

by

Isaac Chavez, B.S.

THESIS

Presented to the Faculty of the Graduate School of
The University of Texas at Austin
in Partial Fulfillment
of the Requirements
for the Degree of

MASTER OF ARTS

THE UNIVERSITY OF TEXAS AT AUSTIN

August 2010

Dedicado a mi familia. Gracias por todo su amor y apoyo.

Acknowledgments

First and foremost, I want to thank the biggest influence in my college career, my supervisor Mark G. Raizen. Mark, you have been more than a supervisor to me; you have been a mentor and friend. You have given me opportunities which I had only dreamed about, and I am extremely grateful. It has been a pleasure working for you in your group, and this is just the beginning of what is to come.

I want to thank my co-workers on the magnetic slower: Adam Libson, Tom Mazur, Dr. Robert Clark, Dr. Edvardas Narevicius, and Christian Parthey. Ed, you pushed me to limits I never thought were possible, and you were always there for me personally and professionally, and I thank you. Adam, I remember working with you since day one, and your extreme knowledge of everything has not only helped my studies in physics but has opened my mind to other topics; thank you for making me a better student. Christian, thank you for your help and guidance on the early stages of the magnetic slower. Tom, you have been a great lab partner and friend. I will never forget the late night study sessions for our core courses, and without you, I wouldn't have been able to get through them; thank you. Finally Rob, you have been a positive influence in and out of the lab. Thank you for being there as a helping hand and talking with me during difficult times.

I would like to thank my co-worker Melissa Jerkins for work on Single-Photon Atomic Sorting. Your work ethic and personality is second to none. You have been a great lab partner and I've enjoyed everyday we have worked together.

I want to thank the rest of the Raizen lab, past and present: Travis Bannerman, Tongcang Li, Kirsten Viering, David Medellin, Jianyong Mo, Simon Kheifets, Francisco Camargo, Daniel Ellsworth, Gabriel Price, Hrishikesh Kelkar, and Christoph Schaeff. You all have made my experience in the Raizen lab the best by providing an atmosphere any graduate student would love.

Last but certainly not least, I would like to thank my family. To my parents Nora and Gonzalo Chavez: your love, support, and guidance has given me the greatest opportunity to become successful. I appreciate everything you have done for me throughout my entire life, and I love you two very much. My brothers, Adrian, Gabriel, and Gonzo, have always encouraged me to try my best and have given me everything I needed to become successful. I want to thank my cousin Frank Chavez for showing me around UT and Austin and for getting me adjusted to college life. Finally, to my best friend Jose Ramirez and my girlfriend Crystal Gonzalez, thank you for being with me every step of the way and enduring the stress and strain with me. Thank you for giving me guidance when I needed it the most.

ISAAC CHAVEZ

The University of Texas at Austin

August 2010

Magnetic Control of Supersonic Beams: Magnetic Slowing to Isotope Separation

Isaac Chavez, M.A.

The University of Texas at Austin, 2010

Supervisor: Mark G. Raizen

General control of atoms and molecules has long been a goal for atomic physicists and physical chemists. Techniques such as laser cooling have been a huge breakthrough in studying ultra cold atoms and BECs. Although laser cooling has been a remarkable tool, it is limited to small group of atoms on the periodic table. A general technique to control and manipulate the entire periodic table has been out of reach until now. In this thesis I describe two methods of general control of atoms in the contexts of stopping supersonic beams and of isotope separation. Both these methods take advantage of high flux supersonic beams and the fact that every atom has a magnetic moment in the ground state or a long-lived excited state which can be manipulated using magnetic field gradients.

The first method uses a series of pulsed electromagnetic coils to slow and stop a supersonic beam of paramagnetic atoms and molecules. We have demonstrated the slowing of metastable neon and molecular oxygen using 64 coils from 446.5 m/s to 55.8 m/s for metastable neon, and from 389 m/s to 83 m/s for molecular oxygen respectively.

The second method is a novel and efficient approach to isotope separation which utilizes the concept of Maxwell's Demon. We call this technique Single-Photon Atomic Sorting as it is closely related to Single-Photon Cooling, a cooling technique developed in our laboratory. Our method uses a laser beam to change the magnetic moment to mass ratio in such a way that the desired isotopes are guided through a multi-pole magnetic field and collected. We show simulation results for various test cases which highlight the general applicability of this method.

Table of Contents

Acknowledgments	v
Abstract	vii
Chapter 1. Introduction	1
Chapter 2. Principle of Operation	4
2.1 Supersonic Beams	4
2.1.1 Even-Lavie Valve	9
2.1.2 DC Discharge	11
2.2 Interaction with Magnetic Fields	12
2.2.1 Atoms in an External Magnetic Field	13
2.2.1.1 Magnetic Guiding	15
2.2.2 Characterization of Magnetic Fields	16
2.2.3 Phase Stability	17
2.3 Maxwell's Demon	20
Chapter 3. Magnetic Slower	22
3.1 Experimental Overview	22
3.1.1 Cooling the Nozzle	22
3.1.2 Coils	23
3.1.3 Chamber and Coil Support	25
3.1.4 Coil Electronics	27
3.1.5 Timing Sequence	31
3.1.6 Field Characterization	32
3.1.7 Detection	36
3.1.7.1 Metastable Neon Detection	36
3.1.7.2 Molecular Oxygen Detection	37
3.2 Results	37
3.2.1 Metastable Neon	37
3.2.2 Molecular Oxygen	41

Chapter 4. Isotope Separation	45
4.1 Current Methods	45
4.2 Single-Photon Atomic Sorting	47
4.2.1 Entrainment	49
4.2.2 Magnetic Guiding	50
4.2.3 Non-Zero Magnetic Moment in Ground State	55
4.2.3.1 Lithium	55
4.2.3.2 Neodymium	59
4.2.4 Zero Magnetic Moment in Ground State	61
4.2.4.1 Calcium	61
Chapter 5. Conclusion	65
5.1 Magnetic Slower	65
5.2 Isotope Separation	66
Appendix A. Spectroscopic Notation	68
A.1 Atoms	68
A.2 Diatomic Molecules	68
Bibliography	71
Vita	77

Chapter 1

Introduction

Controlling and manipulating the motion of neutral atoms has been a goal of atomic physicists since the early 20th century starting with the work of Otto Stern and Walther Gerlach. They used magnetic field gradients produced with permanent magnets to deflect silver atoms from an oven source [1]. This work pioneered the understanding of spin quantization and ultimately the development of quantum mechanics. It was not until the development of lasers in the 1970s, however, that the door was opened for control and manipulation of atoms using light. Since then, the field has made great progress starting with laser cooling and trapping, which led to the formation of a Bose-Einstein condensate [2–4]. Other methods have also been developed, such as buffer gas cooling, which relies on collisions with liquid helium within a dilution refrigerator [5]. Buffer gas cooling has been successful in cooling and trapping many atomic and molecular species. All of these techniques, however, are problematic for general control of atoms. For example, laser cooling and trapping is limited to a small subset of atoms on the periodic table and while buffer gas cooling is general, it is very expensive, complicated to operate, and has limited optical access.

Recently developments have been made to control and slow supersonic beams. These developments include mounting a supersonic nozzle on a spinning rotor, and reflection from a moving crystal [6–8]. The supersonic beam has re-

markable properties; it is a cold, intense beam of atoms with a divergence angle of only a few degrees and a velocity spread of only 1% of the mean velocity [9]. Atoms in gas phase can be seeded with a carrier gas and put directly in a supersonic nozzle, while other species can be entrained into the beam through laser ablation or effusive ovens [10–12]. The ability to entrain gives the supersonic beam a huge advantage over other atom sources. One drawback, however, to supersonic beams is their high velocities, typically on the order of hundreds of meters per second. Mounting the supersonic nozzle on a spinning rotor has been successful in slowing a supersonic beam but entrainment is difficult and is limited to species in gaseous form. Reflection from a receding crystal has demonstrated slowing of a supersonic beam of helium, but no other species has been slowed with this method.

To address the issue of general control, we have developed two new methods for controlling and manipulating paramagnetic atoms. The first, the magnetic slower, uses a supersonic beam as a bright source of atoms and stops them in the laboratory frame using a series of electromagnetic coils [13–15]. The second is a cooling technique called Single-Photon Cooling, which uses informational entropy (Maxwell’s Demon) to efficiently cool trapped species with a single photon [16–18]. Both techniques combined will allow trapping and cooling of any paramagnetic species. This thesis will focus on the magnetic slower portion of these two techniques.

These new methods have also led to practical applications, one being isotope separation. We have developed a new technique to efficiently separate isotopes by utilizing the magnetic moment of the atoms. We call this technique Single-Photon Atomic Sorting, as it is closely related to Single-Photon Cooling.

This method separates a supersonic beam by probing the desired isotope with a laser, and it uses a magnetic guide to perform the separation [19]. Our technique takes advantage of the magnetic moment, which most atoms possess in either the ground state or a long lived excited state.

In this thesis I describe in detail the magnetic slower and Single-Photon Atomic Sorting. The thesis layout is as follows:

Chapter 2 discusses the underlying principles of both the magnetic slower and isotope separation. It describes in detail the operation of the supersonic beam and atomic interactions with external magnetic fields. It highlights how one can control and manipulate paramagnetic atoms. A brief discussion of Maxwell's Demon and its relevance to informational entropy is given and related to our isotope separation technique.

Chapter 3 discusses the experimental setup and results of the magnetic slower. The 64 stage coil setup is described in detail, as are the driver electronics and magnetic field characterizations. We show slowing results of metastable neon and molecular oxygen.

In Chapter 4, I describe the simulation results of Single-Photon Atomic Sorting. We propose two methods of isotope separation, one for atoms with a non-zero magnetic moment in the ground state, and the other for atoms with zero magnetic moment in the ground state. This technique enables separation of almost every isotope on the periodic table.

Finally, a summary and future applications are discussed in Chapter 5.

Chapter 2

Principle of Operation

In this chapter, a thorough analysis of the physical principles of both the magnetic slower and isotope separation will be discussed. We start with a general description of supersonic beams, our Even-Lavie valve, a DC discharge to create our metastable neon, and a description of atomic interactions with external magnetic fields. We also discuss phase stability and outline a method used to characterize our magnetic coils using Faraday rotation. Finally a brief discussion of Maxwell's Demon as applied to Single-Photon Atomic Sorting is discussed.

2.1 Supersonic Beams

Atomic beams of atoms and molecules are generally produced by allowing a gas from a high-pressure reservoir to escape through an aperture into a low-pressure region. Two key regimes are realized: the effusive regime and the supersonic regime. In the effusive regime the mean free path of the atoms is much larger than the aperture through which the atoms escape. The velocity distribution of such a beam is as follows [10]

$$f(v) = \frac{4}{\sqrt{\pi}} \left(\frac{m}{2kT} \right)^{3/2} v^2 \exp \left(\frac{-mv^2}{2kT} \right) \quad (2.1)$$

where m is the mass of a single particle, v is its velocity, k is Boltzmann's constant, and T is the temperature. The most probable speed v_w defined as the speed at

which the distribution function has its maximum value, is

$$v_w = \sqrt{\frac{2kT}{m}} = 1.2895 \times 10^2 \sqrt{\frac{T}{M}} \quad (2.2)$$

where M is the molecular weight of the atom and the resulting speed in is m/s.

The velocity spread of the distribution is given as

$$\sigma_v = \sqrt{\frac{kT}{m}} = 91.18 \sqrt{\frac{T}{M}} \quad (2.3)$$

with σ_v in units of m/s. For neon at 300 K the most probable velocity is 500 m/s with a beam spread of 350 m/s. The velocity spread is about 70% of the most probable velocity, and is therefore very broad.

The mean free path of the particles is proportional to the temperature and inversely proportional to the pressure. Therefore, increasing the pressure of the gas will decrease the mean free path. When the mean free path becomes comparable to the escaping aperture one must consider collisions during the gas dynamic expansion. When the mean free path becomes smaller than the escaping aperture, the gas expansion becomes supersonic. The supersonic regime is very important to producing high-intensity, low-divergence atomic or molecular beam sources. The basis of describing the dynamic flows of the supersonic beam begin with three conservation equations given in one dimension:

1) Continuity equation

$$\frac{dw}{w} + \frac{d\rho}{\rho} + \frac{dA}{A} = 0 \quad (2.4)$$

2) Momentum equation

$$w dw = -\frac{dP}{\rho} \quad (2.5)$$

3) Energy equation

$$w dw + dh = 0 \quad (2.6)$$

where w is the velocity of the gas, ρ is the gas density, A is the cross-sectional area of the nozzle, P is the pressure of the gas, and h is the enthalpy per unit mass defined as

$$h = e + \frac{P}{\rho} = e + \frac{RT}{M} \quad (2.7)$$

where e is the internal energy of the atom and R is the gas constant. Using the above equations and the ideal gas law one can derive a simple equation which describes the change of flow velocity w through a passage with a changing cross-sectional area [10].

$$\frac{dA}{A} + \frac{dw}{w}(1 - M_a^2) = 0 \quad (2.8)$$

where M_a is the Mach number defined as: $M_a = \frac{w}{c}$. The Mach number is the ratio of the flow velocity w , to the speed of sound c in the medium. From equation 2.8, for $M_a < 1$ ($w < c$), the flow velocity increases with decreasing area and decreases with increasing area. For a supersonic flow velocity $w > c$ ($M_a > 1$) the opposite holds. Equation 2.8 gives insight into the type of nozzle that is needed to obtain a supersonic beam namely a convergent-divergent nozzle or a Laval nozzle named after Swedish engineer De Laval.

By integrating the energy equation 2.6, the flow velocities at two different positions labeled 1, 2 are related by:

$$\frac{w_2^2 - w_1^2}{2} = h_2 - h_1 = \int_{T_1}^{T_2} c_p dT = c_p T_1 (1 - T_2/T_1) \quad (2.9)$$

Where c_p is the specific heat at constant pressure. The specific heats at constant

pressure and volume are defined as:

$$c_v = \left(\frac{\partial e}{\partial T} \right)_v = \left(\frac{de}{dT} \right)_v \quad (2.10)$$

$$c_p = \left(\frac{\partial h}{\partial T} \right)_p = \left(\frac{dh}{dT} \right)_p \quad (2.11)$$

The partial derivative can be replaced by an ordinary derivative for an ideal gas. Differentiating equation 2.7 and using 2.10 and 2.11 gives this relation between specific heats,

$$c_p = c_v + \frac{R}{M} \quad (2.12)$$

and by inserting $\kappa=c_p/c_v$ into 2.12 gives:

$$c_v = \frac{1}{\kappa - 1} \frac{R}{M} \quad (2.13)$$

and

$$c_p = \frac{\kappa}{\kappa - 1} \frac{R}{M} \quad (2.14)$$

Substituting equation 2.14 into equation 2.9 taking into account stagnation pressure P_0 and temperature T_0 where $w_1 \approx 0$, and Point 2 denotes any other point in the flow (i.e. $w_2 = w$) the velocity of the supersonic beam is

$$w = \sqrt{2 \frac{\kappa}{\kappa - 1} \frac{RT_0}{M} \left(1 - \frac{T}{T_0} \right)} \quad (2.15)$$

This is a very useful relation as it gives a relationship between the velocity and the mass of the atom. This means a heavier gas will give a lower initial beam velocity. Expressing equation 2.15 in terms of Mach number and solving for temperature yields:

$$T = \frac{T_0}{1 + \frac{\kappa-1}{2} M_a^2} \quad (2.16)$$

It is clear from equation 2.16 that a higher Mach number will produce a colder beam. Experimentally it is often convenient to rewrite the Mach number in terms of the speed ratio. The speed ratio S is the ratio between the flow velocity w and the most probable velocity v_w namely,

$$S = \frac{w}{v_w} = \sqrt{\frac{\kappa}{2}} M \quad (2.17)$$

Now the temperature can be written as

$$T = \frac{T_0}{1 + \frac{2}{5} S^2} \quad (2.18)$$

In practice the speed ratio can be calculated by fitting the pulse distribution to a Gaussian curve centered at time t . The relation is given by [9]:

$$S = 2\sqrt{2\ln(2)} \frac{t}{\Delta t_{FWHM}} \quad (2.19)$$

where Δt_{FWHM} is the full width half maximum of the distribution. This relation relates experimental time of flights of the supersonic beam and its corresponding temperature.

Since we are interested in slowing and controlling supersonic beams of atoms, it is advantageous to start with a beam with the lowest possible initial velocity. This is done in two ways: first to cool the nozzle to lower the gas temperature, and second to seed the supersonic beam with a heavier “carrier gas”. For instance we cool our nozzle to 77 K for neon for which the mean beam velocity is 400 m/s. By contrast, neon at 300 K will give a beam velocity of 800 m/s. Care must be taken when cooling a supersonic nozzle to prevent clustering and condensation which will degrade the performance of the nozzle. Seeding two

species together is a great way of reducing mean velocities. As equation 2.15 dictates, a heavier mass will have a lower beam velocity. For instance seeding helium into a neon carrier gas at 77 K at a ratio of 1:10, will produce a beam at 500 m/s. This is a huge advantage as opposed to a pure beam of helium which has a mean beam velocity of 900 m/s at 77 K. When slowing molecular oxygen, we seed oxygen with krypton for this purpose.

Supersonic beams are a great source of atoms but are only applicable to gaseous atoms at room temperature. To introduce any other species into a supersonic beam, an external source must be used. This process is called “entrainment” which involves an effusive beam of atoms created in an oven being crossed with the supersonic beam, or laser ablation which uses a high-power laser to evaporate atoms off a solid target next to the aperture of the nozzle [10]. The two processes must occur near the entrance of the nozzle where densities are extremely high, and thus the external atoms have a greater chance of being picked up in the supersonic flow. Since the beam is still collisional, the entrained gas will thermalize with the supersonic beam and cool through adiabatic expansion, and take on the properties of the supersonic beam. This allows any type of species to be introduced into a supersonic flow without putting the gas directly into the nozzle.

2.1.1 Even-Lavie Valve

We use an high-intensity, cryogenic, pulsed Even-Lavie supersonic nozzle [9, 20]. The properties of this nozzle are remarkable with pulses as short as 10 μ s FWHM, and a repetition of 40 Hz (nozzles with repetition rates of 1 kHz are also available), with cryogenic (77 K) operation. The nozzle emits a flux of $\Phi = 4 \times 10^{23}$ atoms/s/sr with a divergence of 7° half angle. The valve produces the shortest

pulse and gives higher fluxes than other commercially available supersonic nozzle.

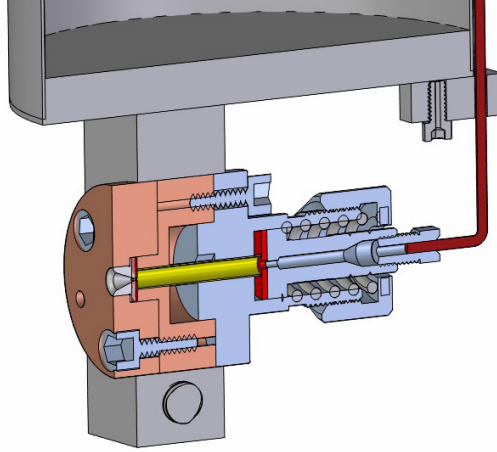


Figure 2.1: The Even-Lavie cryogenic supersonic valve. A cross-sectional view is taken to give a better view. The nozzle assembly is attached to a cryostat and is cooled. The mechanism for the valve (plunger and spring) is enclosed in the yellow tube and sealed with two kapton washers in red. The assembly is held by a large spring in the back of the nozzle. Gas is supplied to the nozzle by a 1/16" stainless steel tube shown here in red at the back of the assembly.

The nozzle is backed with a plunger which is held in place with a spring. An electromagnetic coil surrounds the plunger and produces a magnetic field of 2.5 T for 20 μs . The electromagnetic coil pulls the plunger back opening the nozzle. The nozzle is pulsed on and off by pulsing current to the electromagnetic coil. The nozzle seals with two kapton washers (front and back). Gas is supplied to the back of the nozzle with a 1/16" stainless steel tube. The assembly is held in place by a large spring and nut in the back of the nozzle. The nozzle is clamped at the bottom of a tank for cryogenic use. The complete assembly and cryostat are shown in Figure 2.1.

2.1.2 DC Discharge

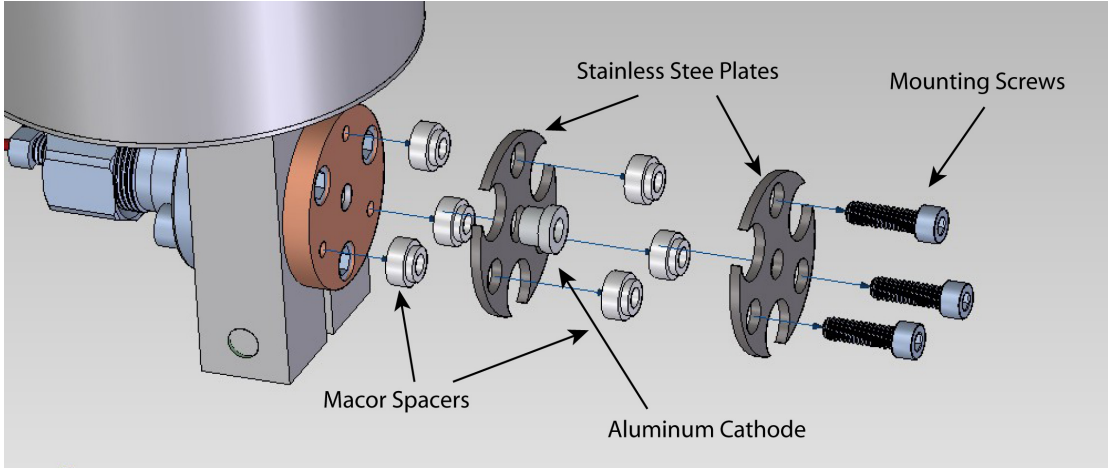


Figure 2.2: Schematic view of the DC discharge. The discharge is mounted on the front copper plate of the nozzle. Wire leads are spot welded to the stainless steel plates to provide high voltage and ground. It is held together with the mounting screws.

We use a direct current (DC) discharge between two stainless steel plates to create a metastable beam of neon in the 3P_2 state. The discharge produces a beam of electrons between the plates which create metastables through electron-beam bombardment [21]. The discharge consists of two stainless steel plate electrodes, an aluminum cathode, and macor spacers all mounted to the front copper plate of the nozzle (shown in Figure 2.2). The inner stainless plate and aluminum cathode are held at a voltage of 1 kV (pulsed) while the outer stainless steel plate is held at ground. With our electronics we can pulse up to a voltage of 2 kV. We use a capacitor bank of 20, 5.6 nF capacitors (0.112 pF total capacitance) charged through a 10 M Ω resistor limiting the current to 0.2 mA. We discharge the capacitors through a fast high voltage transistor switch (Behlke, HTS 31-03-

GSM) through a $100\ \Omega$ resistor. The discharge is initiated and stabilized with a tungsten filament held at 3.5 A and -100 V (not shown in Figure 2.2) and is placed as close to the front of the discharge as possible without blocking the beam line. Typical discharge pulse widths are about $3\ \mu\text{s}$ with a $100\ \mu\text{s}$ delay from the nozzle pulse with a repetition rate as high as 5 Hz.

The stainless steel plates are 1.182" in diameter and 0.06" thick. The macor spacers provide a 0.118" space between the two plates. The aluminum cathode has a inner bore of 0.157" and is spaced 0.039" from the nozzle. The discharge occurs between the ground stainless steel plate and the aluminum cathode which can be viewed through a view-port. Figure 2.3 shows a picture of the discharge during a pulse.

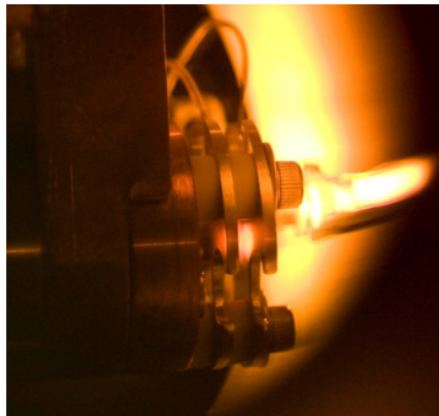


Figure 2.3: A picture of the DC discharge during a pulse.

2.2 Interaction with Magnetic Fields

The principle of the magnetic slower is based on the Zeeman effect, similar to the Stark decelerator based on the DC Stark shift [22–25]. Atoms or molecules

with a non-zero total angular momentum will split their internal energy into magnetic sublevels in the presence of a magnetic field. Depending on the magnetic projection of the atom, it is said to be a high- or low-field seeking atom once it enters a magnetic field. Atoms which are attracted towards regions of low (high) magnetic field are called low-field seeking (high-field seeking) atoms. Our design for the magnetic slower uses electromagnetic coils which are optimized for low-field seeking atoms. In the case of isotope separation the low-field seeking atoms (high-field seeking atoms) are guided (anti-guided) through the multi-pole magnetic field.

When a low-field seeking atom enters the bore of our coil it will lose kinetic energy as it compensates for the Zeeman shift and thus feel a magnetic potential “hill”. If the coil were left on, the atom will exit the coil and regain the lost kinetic energy and leave with the same velocity it entered with. However if the coil is switched off when the atom enters, the atom will lose kinetic energy equal to the Zeeman shift and decelerate. By having multiple coils the atom can lose all of its kinetic energy and thus be brought to rest in the laboratory frame without affecting the temperature of the atoms. The atoms will be sufficiently slow enough to be trapped with a magnetic trap.

2.2.1 Atoms in an External Magnetic Field

Atoms experience a change in internal energy due to their magnetic moment within a magnetic field. Atoms within a weak magnetic field (weak field limit) will experience a shift in energy equal to

$$\Delta E = -m_j g_j \mu_B B \tag{2.20}$$

where m_j is the projection of the total angular momentum on the quantization axis, g_j is the Landé g-factor, μ_B is the Bohr magneton, and B is the component of the magnetic field along the quantization axis. The atom's magnetic moment will adiabatically follow the direction of the magnetic field as long as the atom's Larmor frequency is much greater than the rate of change of the magnetic field.

The Landé g-factor is given by

$$g_j = 1 + \frac{J(J+1) + S(S+1) - L(L+1)}{2J(J+1)} \quad (2.21)$$

where J is the total angular momentum ($J = S + L$), S is the total spin, and L is the total orbital angular momentum.

When the energy shift becomes large enough to exceed the spin-orbit splitting, atoms enter the strong field limit or Paschen-Back regime. Here J is no longer a good quantum number, so the energy splitting is given by

$$\Delta E = (m_l + 2m_s)\mu_B B \quad (2.22)$$

where m_l and m_s are the magnetic quantum numbers for orbital and spin angular momentum respectively. We take advantage of the fact that every atom with a magnetic moment will experience an energy shift which then can be removed using our coils.

The force on an atom as it enters a magnetic field gradient is equal to:

$$F = \mu_B g_j m_j \nabla B \quad (2.23)$$

where ∇B is the magnetic field gradient. Substituting Newton's second law into equation 2.23 gives an expression for the deceleration of an atom in a magnetic

field gradient

$$\ddot{x} = \frac{\mu_B g_J m_J \nabla B}{m} \quad (2.24)$$

This equation is then integrated to find the equation of motion for an atom in a magnetic field gradient. For a given magnetic field gradient the effectiveness of the slower is determined by the magnetic moment to mass ratio of an atom ($\frac{\mu_B g_J m_J}{m}$). Atoms with low magnetic moment to mass ratio need more coils to stop the supersonic beam than atoms with high magnetic to mass ratios. For example metastable neon in the 3P_2 state has a magnetic moment to mass ratio of $3\mu_B/20$ (for $m_j = 2$), and hydrogen in the ground state has $1\mu_B/1$. Thus hydrogen can be slowed with fewer coils than metastable neon.

For molecules, the interaction with magnetic fields is the same as for atoms, however different notation is used to account for parity, and additional angular momentum (Appendix A shows spectroscopic notation for both atoms and diatomic molecules). Suppose molecular oxygen is in the $^3\Sigma_g^-$ triplet ($S = 1$) ground state. Nuclear statistics forbid the $K = 0, 2, 4$ rotational levels of $^{16}\text{O}_2$ so the lowest rotational state for molecular oxygen is $K = 1$. For oxygen we want to slow the $K = 1, J = 2, M_j = 2$ sublevel state which has the highest magnetic moment in the low- and high-field regimes, where the magnetic moment is approximately equal to 1.8 Bohr magnetons [26].

2.2.1.1 Magnetic Guiding

This section will discuss how atoms can be guided using a multipole magnetic configuration. This is relevant for isotope separation (Chapter 4). When an atom enters the magnetic guide it will experience a force due to the magnetic field

gradient (eq 2.23). The strength of the force will be determined by how strong the magnetic field gradients are.

The magnetic field (and resulting gradients) for an ideal multipole only depends on the distance from the center ρ [27]

$$|B(\rho, \phi)| = B_n \left(\frac{\rho}{\rho_1} \right)^{n-1} \quad (2.25)$$

Where B_n is the strength of the magnetic field at the outer edge of the magnets, ρ_1 is the radius of the guide (distance to the magnet), and n is the pole number ($n = 2$ for quadrupole, $n = 3$ for hexapole). As seen by equation 2.25 a quadrupole will have a linear dependence on ρ , which means ∇B will be constant over ρ . Likewise for the hexapole it will have a ρ^2 dependence, and ∇B will be linear in ρ .

The forces experienced by the atom will be different for both quadrupole and hexapole because of the dependence on ρ . Low-field seeking atoms will be guided through both configurations because of the magnetic field minimum is the center of the each multipole. Both of these multipoles however, will have their own distinct advantage for isotope separation. Each multipole will be constructed with a different number of magnets which will be discussed in detail in section 4.2.2.

2.2.2 Characterization of Magnetic Fields

The method we use to characterize the magnetic fields within our coils is Faraday rotation. When a laser beam with a certain linear polarization goes into

a Faraday crystal with an applied magnetic field, the polarization will rotate. The relationship between the rotation and the applied magnetic field is

$$\beta = VBd \tag{2.26}$$

where β is the rotation of polarization in radians, V is the Verdet constant of the crystal, B is the magnetic field, and d is the distance the light travels in the crystal [28].

In our experiment we use a terbium gallium garnet crystal (TGG) which has a Verdet constant of $|V| = 134 \text{ rad T}^{-1} \text{ m}^{-1}$, with anti-reflection coating for 633 nm at room temperature. Our crystal is supplied by Northrop Grumman.

2.2.3 Phase Stability

The magnetic slower can only select a certain velocity distribution within the main supersonic beam. The cluster of atoms that can be slowed is said to be phase stable through the entire slower. We use phase stability in a similar form as the Stark decelerator [25], but the concept dates back to charged-particle accelerators [29].

In Figure 2.4 we show potential hills similar to what an atom will experience through the slower. For simplicity only two coils are shown. The point of highest magnetic field is denoted with phase $\phi = 90^\circ$ and the point where the magnetic field is at the lowest is denoted with phase $\phi = 0^\circ$. These positions in real space correspond to the center of the coil ($\phi = 90^\circ$) and the point half way between two coils ($\phi = 0^\circ$). This is only a pictorial representation of the magnetic profiles, the actual experimental profiles are given in section 3.1.6.

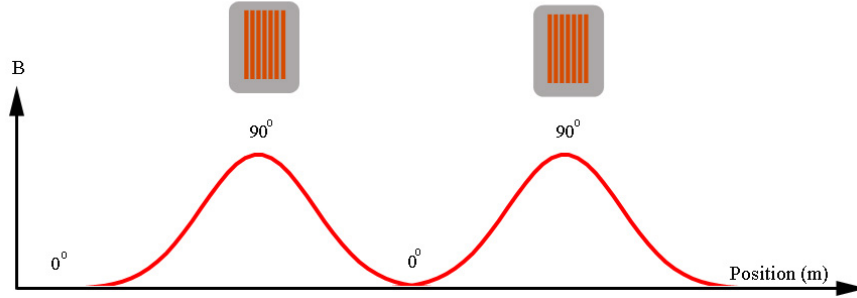


Figure 2.4: Schematic of the magnetic potentials and coils. The highest magnetic potential at the center of the coil represents a phase of $\phi = 90^\circ$ and the lowest magnetic potential at half way between two coils is phase $\phi = 0^\circ$.

The amount of slowing the atom experiences depends on where the atom is relative to the coil when the coil is switched off. We tune our experiment to the synchronous atom which corresponds to the atom in the center of the distribution. This atom is denoted in green in Figure 2.5. In an idealized coil with instantaneous switch off time, a phase of $\phi = 90^\circ$ will be the phase which will remove the most energy from the synchronous atoms. However, this is not ideal for capturing the largest number of atoms because atoms which are faster will be ahead in position and will fall further away from the synchronous atom as shown in Figure 2.5b and c. The faster atom has more energy than the synchronous atom before it enters the coil and will be slowed less than the synchronous atom causing the faster atoms to be even faster in velocity and eventually fall out of phase with the synchronous atom. Because of this, we want to switch the coil off when the synchronous atom is climbing the magnetic potential as seen in Figure 2.5a. This way the faster atoms

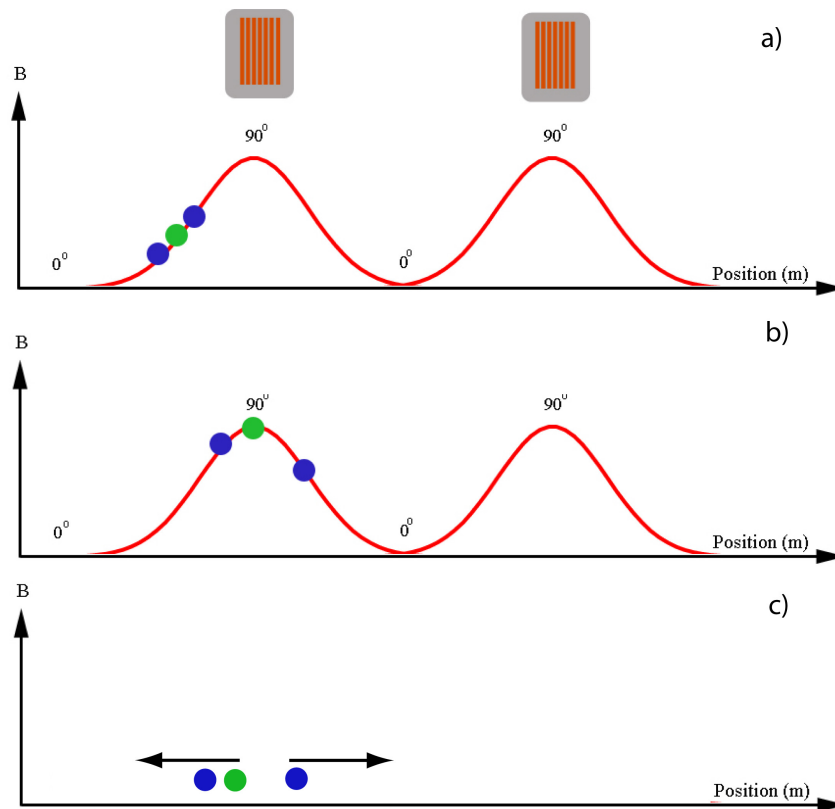


Figure 2.5: a) Atoms entering the coil, b) atoms at the highest peak of the potential, c) Atoms falling out of sync when switched off at $\phi = 90^\circ$. The synchronous atom is shown in green and represents the center of the distribution. This picture assumes instantaneous switching of the coils.

will be higher up the potential hill and will have more kinetic energy removed causing them to fall into place with the synchronous atom. Likewise slower atoms will experience less slowing than the synchronous atom thus causing them to catch up. The group of atoms which are slowed with the synchronous atom are said to be “phase stable” throughout the slower. However this also means that the amount of energy removed is not as much as when the coil is at phase $\phi = 90^\circ$. To compensate for this we simply add more coils to reach the desired final velocity.

Our slower however, doesn't have instantaneous switching so this complicates how the atoms experience the magnetic potential. It is no longer true that a phase of $\phi = 90^\circ$ will provide the highest slowing efficiency but the switching is finite and is the same to all atoms so the above argument still holds. In our experiment phase is the one parameter we adjust to get different final velocities.

2.3 Maxwell's Demon

In 1867 James Clerk Maxwell proposed a thought experiment in which an intelligent “finite being”, if under the correct circumstances, could potentially violate the second law of thermodynamics [30]. Lord Kelvin later dubbed this “being” as Maxwell's Demon [31]. Maxwell's argument is as follows: suppose we have a box filled with molecules with a partition (door) in the center operated by the demon. The demon will then proceed to open the door to allow molecules with a large velocity to enter one side of the box, but then close the door for molecules with lower velocity. As time went on, the demon would then segregate the fast and slow molecules, thus lowering the entropy of the system [32], in clear violation of the second law.

It wasn't until 1929 when Leo Szilard [33], and later work by Shannon and Brillouin [34, 35], showed that the information the demon gained carried entropy. It turns out the informational entropy gained by the demon exactly cancels out the entropy gained from sorting, thus saving the second law.

In our laboratory we have experimentally verified an optical realization of Maxwell's Demon with Single-Photon Cooling [16–18]. This technique uses a laser beam as its demon, which is swept across a cloud of trapped atoms. The knowledge gained by the laser (demon) is the single photon absorbed by the atom then spontaneously scattered. The laser catches each atom at its classical turning point, and changes its internal state by scattering the photon, and is trapped within an optical trap. The atoms transferred in the optical trap have been cooled as a result of this process.

Single-Photon Atomic Sorting works in analogy to Single-Photon Cooling. The desired isotope passing through the laser beam will scatter a photon changing its internal state enabling it to be separated. This separation lowers the disorder of the atomic beam thus lowering the entropy, but the entropy of the laser beam is increased to offset that of the atomic beam. Using information entropy to separate isotopes will be extremely efficient, as it was for cooling atoms using Single-Photon Cooling.

Chapter 3

Magnetic Slower

In this chapter we discuss the magnetic slower. A 64 stage slower and associated driver electronics are discussed. A thorough analysis of the field characterization using Faraday rotation and finite element analysis are shown. Finally, experimental results for both metastable neon and molecular oxygen are presented. In parallel to our work slowing of hydrogen and deuterium has also been realized [36, 37].

3.1 Experimental Overview

3.1.1 Cooling the Nozzle

For both metastable neon and molecular oxygen we cool the nozzle to reduce the initial beam velocity. For metastable neon we can directly pour liquid nitrogen into the cryostat to cool the nozzle. We slowly pour a little liquid nitrogen into the cryostat and let the nozzle cool down. We monitor the temperature using a thermo-couple attached to the cryostat on the vacuum side. It takes about 45 minutes to completely cool the nozzle down to liquid nitrogen temperature. During the entire cool down we pulse the nozzle at 5 Hz to ensure no condensation builds up inside the nozzle which prevents the nozzle from clogging. If the nozzle clogs, we stop pouring liquid nitrogen and blow air down the cryostat to warm it until the nozzle is no longer clogged and then we proceed to cool the nozzle again.

Once the nozzle is down to 77 K we fill the cryostat and stop pulsing the nozzle without fear of clogging.

For cooling of molecular oxygen we cannot pour liquid nitrogen directly into the cryostat because the boiling point of oxygen is 90.19 K, which is hotter than the temperature of liquid nitrogen. This means that oxygen will condense at these temperatures. We regulate the temperature of the nozzle by flowing cold nitrogen gas into the cryostat. We fill a 31 liter dewar and add a variable heat load via a 8Ω , 50 W resistor inserted into the liquid nitrogen. An insulated stainless steel tube sealed with a rubber stopper is placed at the exit of the dewar to direct the boil off to the cryostat of the nozzle. By adjusting the resistor current we can control the boil off rate, and the quantity of cold gas entering the cryostat, and thus control its temperature. Great care must be taken with this method because the resistor can burn if it is not submerged in the liquid nitrogen. We found with our setup we had to add liquid nitrogen to the dewar every hour to ensure the resistor remained submerged.

3.1.2 Coils

The coils are 5 x 6, 500 μm thick copper windings. The coils are wound around a thin vespel cylinder (3 mm outer diameter 100 μm thick) and sandwiched between two permendur caps (Figure 3.1a). Two kapton washers (150 μm thick) serve to protect the coil from scratches that will short the coil to the permendur or the steel case. The entire coil assembly is held together with UHV epoxy within a steel case. A notch in the case gives a space for the leads of the coil to come out.

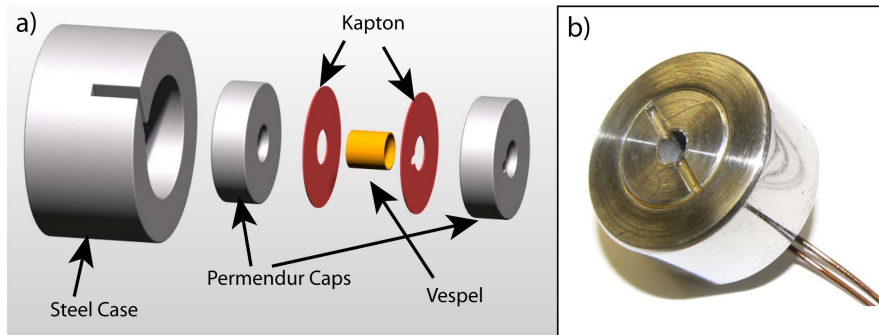


Figure 3.1: a) Schematic of the coil. The coil is held together by two permendur caps encased within a steel case. The coil (not shown) is wound around the vespel cylinder and protected from scratches by the kapton washers. The whole assembly is held together by UHV epoxy. b) Picture of the finished coil.

To make every coil as uniform as possible an array of tools and teflon molds were made to help with the assembly. First, everything is wound over a teflon rod 3 mm in diameter (the permendur caps, kapton washers and coil are sandwiched together). The teflon rod is embedded in a teflon block which serves as material to clamp the whole assembly. The steel case is then put over the entire assembly making a dry fit of the completed coil. Once the steel case is on, the outer permendur cap and kapton washer are removed to allow for epoxy to flow in. We used a two part vacuum epoxy from Epoxy Technology (Epo-Tek H77). The epoxy is mixed and heated to about 50 °C with a heat gun to allow the epoxy to flow better into the coil winding. Once the epoxy is applied the kapton washer and permendur cap are replaced and clamped using a C-clamp. The whole assembly with clamps included are placed in an oven for 3 hours at 150 °C so the epoxy can cure. The coils are then removed from the C-clamps and sanded to remove any excess epoxy. Throughout the process, great care is taken to prevent

scratching. In addition, polarity of the coils must be kept the same throughout the process. To test the coil for shorts, we placed the coil in a beaker of methanol to measure the resistance between the methanol and one of the coil leads. If a resistance is measured the coil is deemed to have a short and is discarded. Every coil is tested this way. A picture of the finished coil is shown in Figure 3.1b.

3.1.3 Chamber and Coil Support

The coil support and slower tube are shown in Figure 3.2. This figure shows the back end of the experiment without the nozzle chamber. The nozzle chamber is where the supersonic nozzle, discharge (for metastable neon), and skimmer are placed. The skimmer is 5 mm in diameter, 50 mm in length, and is placed 300 mm away from the nozzle. The skimmer serves two purposes: to provide differential pumping between the nozzle and slower chamber and to break up shock waves created within the supersonic expansion. We use two, 300 l/s Leybold pumps for the nozzle chamber and one 550 l/s Varian pump for the slower chamber. The pressure in the nozzle chamber is 10^{-9} torr with the nozzle off and 10^{-6} torr with the nozzle pulsing at 5 Hz. The pressure in the slower chamber is 10^{-9} torr but we find that pulsing the coils increased the background pressure. To keep the pressure in the chamber low (10^{-9} torr) we trigger the coils at a repetition rate of 0.075 Hz.

A 2.75" vacuum bellow is used to align the slower chamber to the nozzle chamber. We use a telescope to align the two chambers together using crosshairs mounted on the end of the vacuum tube. The slower chamber consists of the coils, coil holder, electrical feedthroughs, and detector. The coils are screwed onto a monolithic support by an aluminum cap with vented screws (pictured in

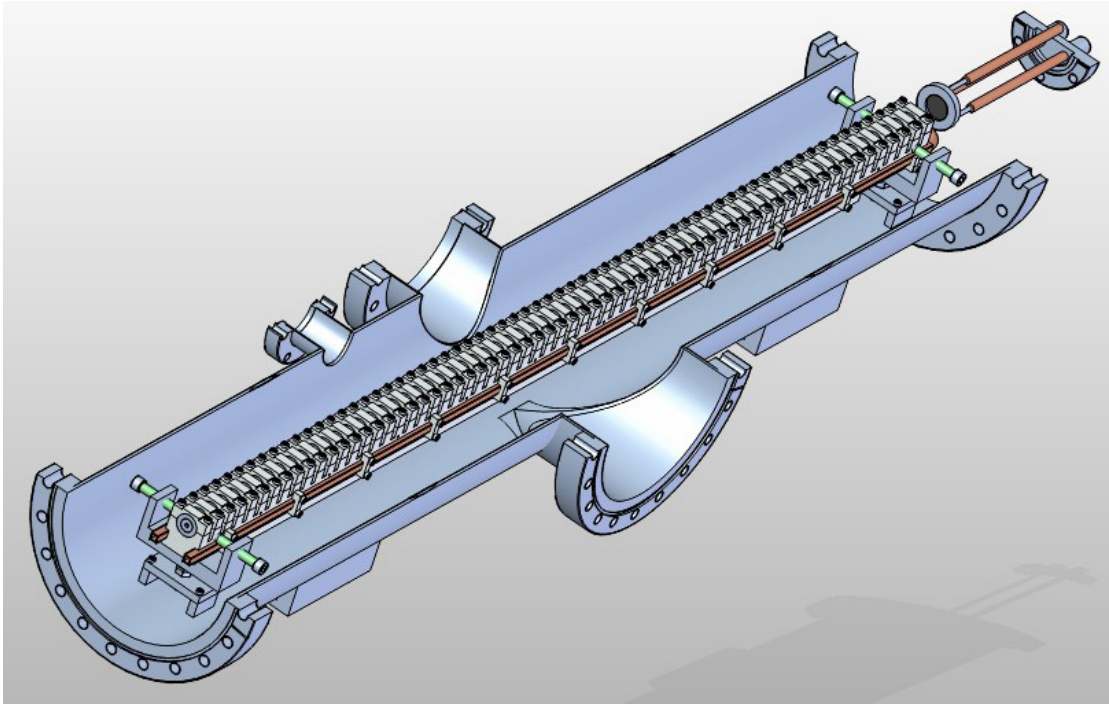


Figure 3.2: 3D view of the coil support and MCP within the vacuum tube. The coils are held into place with a aluminum cap and screwed into the monolithic support. The MCP is shown at the end which is used to detect metastable neon.

Figure 3.3). Each coil is spaced 1.4 cm away from the adjacent coil. The coil support is 89.77 cm long and has a square 1/4" copper tubing attached to provide water cooling to the coils. The coil support rests on a stainless steel translation stage which in turn is mounted on a bracket which is welded into the chamber. Two 1/4-20 screws with round tips are used for aligning and ultimately to secure the coil holder and translation stage in place. Electrical connection for the coils is preserved by feedthroughs which are 50 pin D-sub PEEK connectors (from Accuglass). The leads inside vacuum are wrapped with a PEEK spiral material which prevents the coil leads from scratching against the coil holder. Finally at

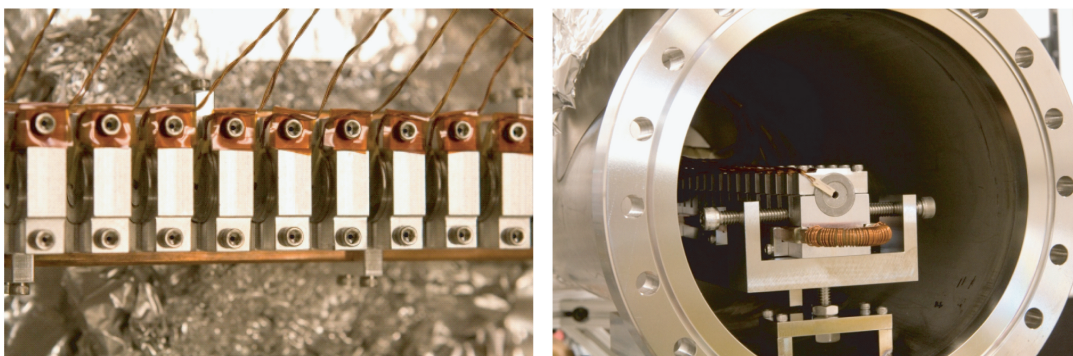


Figure 3.3: Pictures of the coil holder (left) and the coils in vacuum (right). The coil support is mounted on a stainless steel bracket which is welded to the vacuum chamber.

the end of the coils is the micro-channel-plate (MCP) for detection of metastable neon. For detection of molecular oxygen we used a quadrupole mass spectrometer. Both detectors were mounted on a welded bellows which is mounted on a 5.08 cm translation stage for measuring beam velocities. Figure 3.4 shows the complete experimental overview including the nozzle chamber.

3.1.4 Coil Electronics

Each coil is driven with a 2.2 mF discharging capacitor. The capacitor is charged to 258 V and the entire resistance of the coil circuit is 0.34Ω , which pushes 750 A of current through the coil. We pulse the coil for $100 \mu\text{s}$ at a repetition of 0.075 Hz. The electronics are the same for both metastable neon and molecular oxygen. Figure 3.5 shows a picture of the individual board which supplies current to one coil. We have 64 of these coils in two electrical boxes.

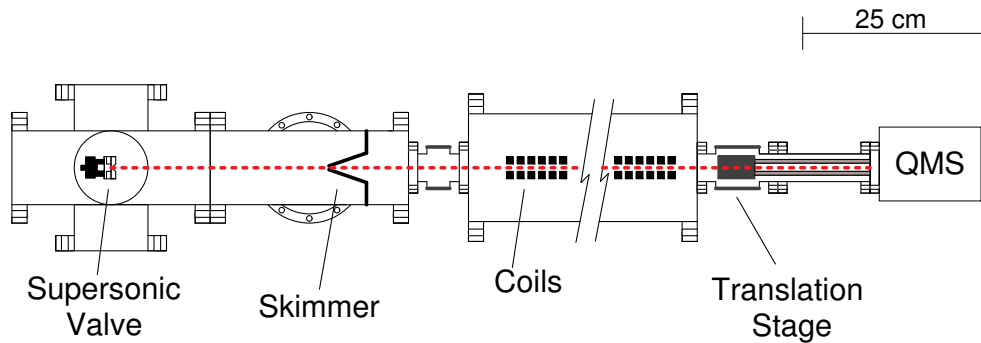


Figure 3.4: Schematic of the experimental setup. The supersonic beam, skimmer, and 64 coils are the same as for metastable neon. We detected molecular oxygen using a quadrupole mass spectrometer (QMS). For metastable neon the QMS is replaced with an MCP and discharge is used on the nozzle. The total length of the experiment is 1.54 m.

We use a high speed, solid state switch (IGBT from Powerex model CM200DY-24A), to provide the fast switching. These IGBTs are rated for high current, high voltage applications. Due to the coil inductance the fast pulse will provide a large voltage spike of 1050 V due to the back emf. For this purpose the IGBT has a huge advantage over MOSFETs which are usually rated for lower voltages. Each IGBT must be driven with its own driver (Powerex BG2A-NF). The IGBT is very useful because it can close and break the circuit very quickly. Since we are able to switch the IGBTs on and off very quickly, these switches are very expensive. We use another low cost, relatively slow switch to isolate the coil from the IGBT. A thyristor is used which can be triggered on but not off, and only closes $40 \mu s$ after current has stopped flowing through the circuit. In order for a coil to trigger each board must simultaneously receive a trigger to each switch. This $40 \mu s$ lag time forces us to trigger adjacent coils on different IGBTs. Figure 3.6 shows the



Figure 3.5: A picture of the individual board for each coil. The coil is fired by passing 258 V through 0.34 Ω total resistance for 100 μs .

component schematic of each individual board. We use 8 IGBTs to run the entire slower in which each IGBT triggers 8 individual coils. We fire the first coil on each IGBT in sequence and then the pattern is repeated for the rest of the coils. This means the 1st and 9th coils are next to each other on the same IGBT. We do this because the timing between the 1st and 9th coil is more than 40 μs which gives enough time for the thyristor on the 1st coil to reset its circuit and prevent the coil from firing multiple times. This method of triggering allows us to put as many coils as we want in our slower on only 8 IGBTs thus making it easily scalable.

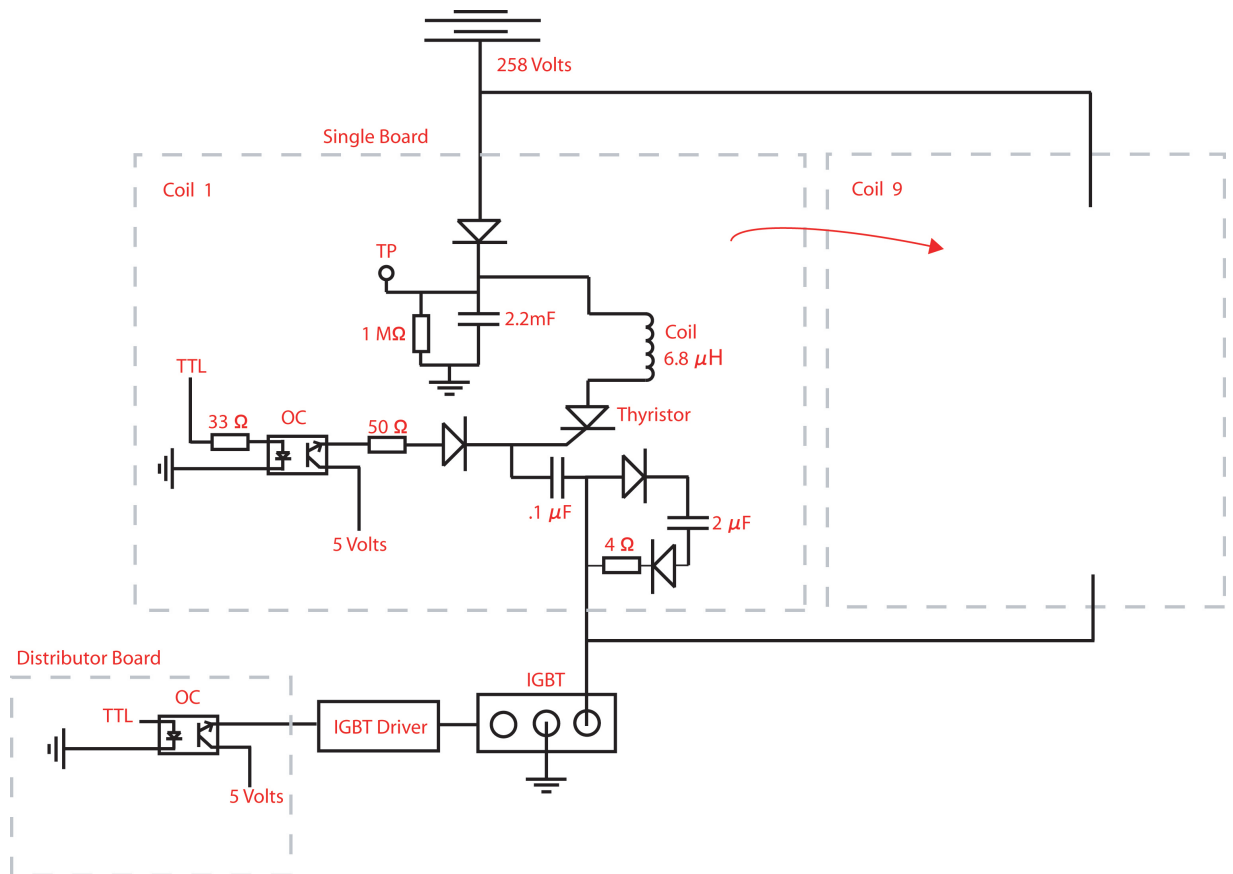


Figure 3.6: Schematic of the individual board setup. Eight individual boards are connected to one IGBT, and 8 IGBTs are used for the entire 64 coil solenoid. The first board on each IGBT fire first (coils 1-8) and repeated for the other coils. The second board on the first IGBT is coil 9 in the sequence. The gray dash line represents different circuit boards. Here TP = test point, OC = optocoupler.

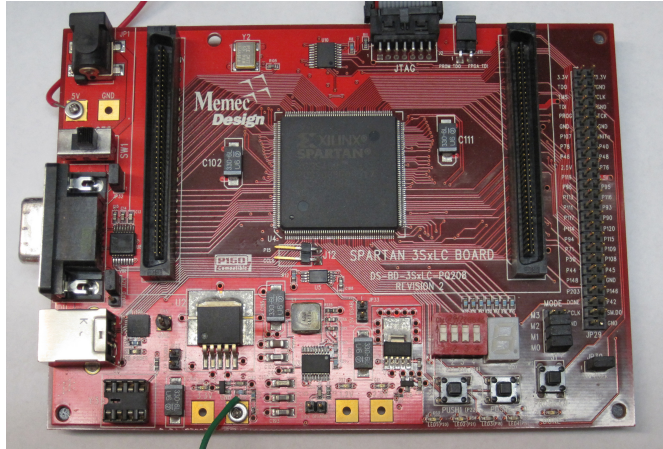


Figure 3.7: Picture of the FPGA board. A timing file is loaded into the board. The distributor board sits on top of the FPGA and buffers the current.

3.1.5 Timing Sequence

To create the timing sequences we integrate the equations of motion of one idealized atom (equation 2.24). This atom has the same velocity as the center atom in our distribution. The timing file is created in MatLab and provides the timing information for each coil. The inputs of the timing file generating program are, the velocity of the distribution and a phase which varies the final velocity of the slowed peak. The timing file is then uploaded to an FPGA which is an inexpensive programmable gate array that can supply multiple outputs. We use a Spartan 3SxLc by Xilinx with 140 digital outputs and has a fast 10 MHz clock which gives a time resolution of 100 ns. This board is then connected to a distributor board (made in house) with D-sub outputs to all the thyristors and IGBTs. The distributor board serves to provide the required current to the switches and isolate the TTL outputs from the FPGA to the IGBTs (through opto-couplers). Figure 3.7 shows a picture of the FPGA board.

3.1.6 Field Characterization

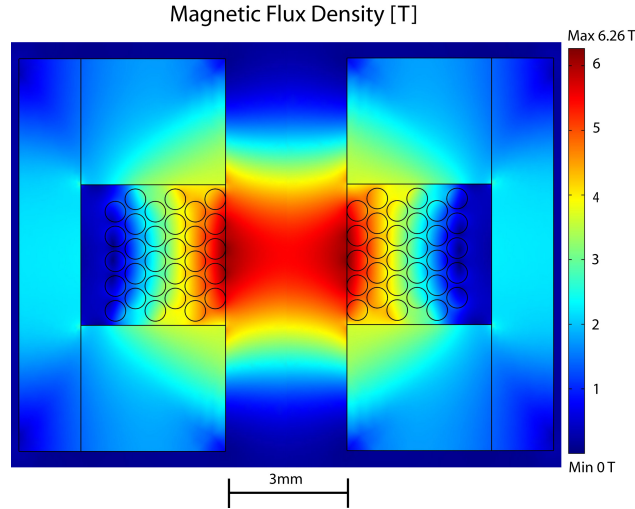


Figure 3.8: A cross sectional view of the coil using finite element analysis. The field in the center of the coil is 5.55 T. The inner diameter is 3 mm. The permendur disks keep the majority of the magnetic flux density lines within the coil.

To determine the magnetic field characteristics we simulate the coil using finite element analysis and compare them to experimental measurement from the Faraday rotator method (discussed in section 2.2.2). Figure 3.8 shows the results of the finite element analysis for our coil. The simulation for the finite element analysis was done using COMSOL Multiphysics. It shows a cross sectional view of the coil and plots the magnetic flux density (T). The peak field is 6.26 T but this is near the coil windings. The peak field in the center of the coil is 5.55 T. Figure 3.9 shows the longitudinal (3.9a) and transverse (3.9b) magnetic field profiles of the coil. The zero in both figures corresponds to the center of the coil. The longitudinal (axial) shows the magnetic “hill” the atoms experience as they enter the coil. It shows a sharp rise from near zero to 5.55 T over a distance of

only 4 mm. The high gradients are caused by a high current and large magnetic saturation from the permendur disks. The transverse direction shows a minimum in the center of the coil, meaning low-field seeking atoms are guided through the coil. This is useful because the atoms are guided throughout the entire slower and do not diverge.

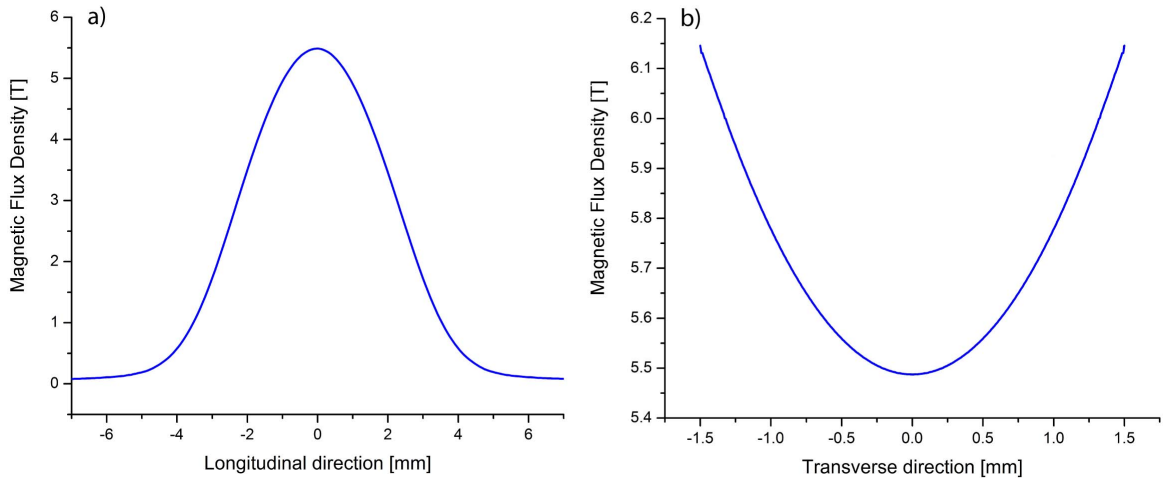


Figure 3.9: These are cross sectional cuts of the magnetic profile from the finite element analysis. a) Longitudinal direction shows the magnetic “hill” the atoms experience through each coil. b) Transverse direction has a minimum in the center of the coil meaning that low-field seeking atoms are guided through the coil.

However these two figures show only spatial information which is not enough to completely characterize the coil. We need temporal information and we get that using the Faraday rotation. Figure 3.10 shows the setup for measuring the temporal response of the coil. We use a HeNe laser (633 nm) which is directed with two mirrors (M1 and M2) into the rotator. A linear polarizing cube (PC1) ensures we only have vertically polarized light going through the coil. A lens with

a focal length of 83 mm is used to focus the laser beam through the coil keeping the waist at $80 \mu\text{m}$ through the length of the coil. The laser then proceeds to go through the TGG crystal inserted into the bore of the coil. Finally the laser goes through the second polarizing cube (PC2) to filter the rotated light. The intensity of the light is measured with a photodiode.

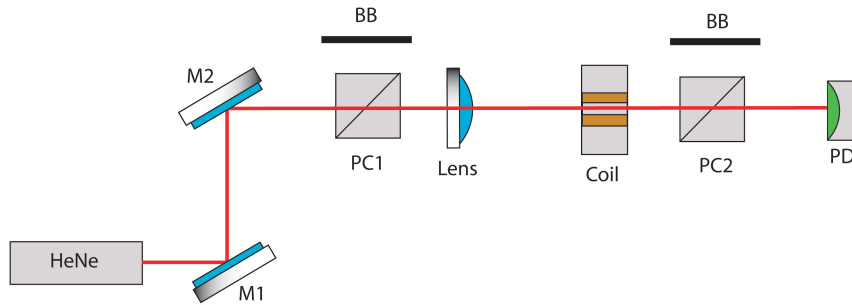


Figure 3.10: Experimental setup of the Faraday rotation. We used a HeNe laser and direct the laser into the coil using two mirrors (M1 and M2). The laser goes through the first polarizing beam cube (PC1) to ensure the polarization is in one direction. Then the laser goes through a 83 mm focal length lens and through the coil with the TGG crystal inside. Finally a second polarizing cube (PC2) filters out the component of the laser which was rotated in the crystal, and the resulting drop in intensity is recorded on the photodiode.

This arrangement of the elements leads to a cosine squared dependence of the intensity on the rotation angle and yields this relation [38],

$$\frac{I}{I_0} = \cos^2 \left[\int_{-d/2}^{d/2} V B(z) dz \right] \quad (3.1)$$

where I_0 is the initial intensity of the beam, d is the length of the crystal, $B(z)$ is the magnetic field along the coil axis and V is the crystal's Verdet constant.

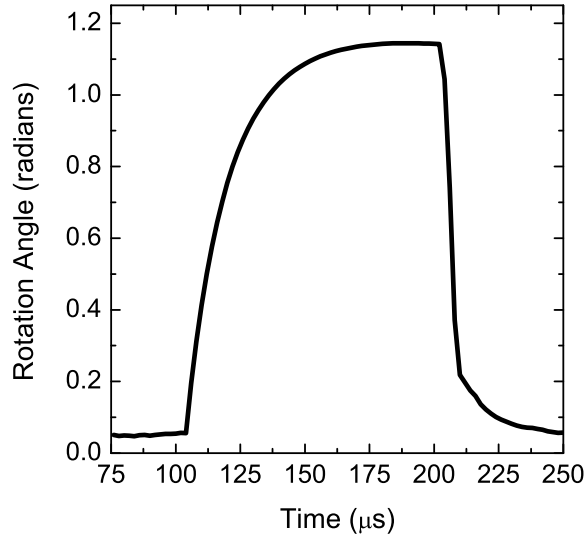


Figure 3.11: This is the temporal profile of a switched coil. This is measured in the oscilloscope and converted from voltage to rotation angle. The peak rotation of 1.1 radians corresponds to a magnetic field of 5.43 T.

Figure 3.11 shows the temporal profile taken with this setup with a 1.4 mm TGG long crystal. We switch from the peak field to about 20 % of the peak field linearly in only 6 μs . The remaining field decays exponentially with a time constant of 17 μs due to eddy currents. We monitor the polarization angle of the beam throughout the switching process. The field measured is the average field over the length of the crystal. To get a more accurate picture of the field profile we use three different length TGG crystals. The results of the measured field is summarized in Table 3.1. We find the average magnetic field to be

$$\bar{B} = 5.21 \pm 0.20\text{T} \quad (3.2)$$

Comparing the average measured peak value of 5.55 T from the finite element analysis finds about a 6 % discrepancy. The finite element analysis assumes perfect windings, so it is not surprising to find some discrepancy with the real coils. Still we find very good agreement between finite element analysis and experimental values of the peak magnetic field.

Table 3.1: The measured magnetic field for each length TGG crystal

TGG length	Measured field [T]
1.40 mm	5.43
2.35 mm	5.05
5.00 mm	5.14

3.1.7 Detection

3.1.7.1 Metastable Neon Detection

The MCP is the detector of choice for detecting metastable species. The type of MCP we use is a chevron configuration made by El Mul Technologies, Ltd.. We create the metastable neon with a DC discharge as discussed in section 2.1.2. When the metastable hits the MCP, the energy released by the metastable is enough to eject an electron from the surface of the MCP. That electron is then accelerated to the electron multiplier and the impact will create secondary electrons. Gains on the MCP can be as high as 10^3 - 10^9 . We use the MCP in conjunction with an external current amplifier (Femto, Variable-Gain high speed amplifier DHPA-100). The MCP is mounted on 1/4" thick, 4.56" long, copper extension rods to place the MCP 4 cm away from the slower exit. The MCP assembly is mounted on a 2.75" blank with three MHV feedthroughs. The blank with the feedthroughs is then mounted onto a translation stage which can trans-

late back 5.08 cm. Every data set is taken twice at two different locations and compared to directly measure the velocity of the slowed peaks.

3.1.7.2 Molecular Oxygen Detection

Molecular oxygen is much different from metastable neon. First a discharge is not needed because ground state molecular oxygen can be slowed directly. However without the metastable energy to liberate electrons, we must use a mass spectrometer for detection. We use a quadrupole mass spectrometer (RGA 100 from Stanford Research Systems) equipped with an electron multiplier. The detector detects all the O₂ in the chamber so it requires an additional pump near the detector to help pump background oxygen out of the chamber. We added a Varian 70 l/s vacuum pump after the coils to help with the added gas load. The output of the mass spectrometer is connected to the external current amplifier just like with metastable neon. The mass spectrometer is mounted on the same translation stage to directly measure the velocity of the slowed peaks.

3.2 Results

3.2.1 Metastable Neon

We show here slowing of metastable neon from $446.5 \text{ m/s} \pm 2.4 \text{ m/s}$ to as low as $55.8 \text{ m/s} \pm 4.7 \text{ m/s}$ with efficiencies as high as 11.9%. This shows a removal of more than 98% of the translation kinetic energy of the atom. Metastable neon has two long lived metastable states which are created in our DC discharge, $^3\text{P}_0$ and $^3\text{P}_2$. The $^3\text{P}_0$ state cannot be slowed because it has a $m_j = 0$ magnetic projection, so we adjust the slower to slow the $^3\text{P}_2$, $m_j = 2$ projection. This state gives the highest magnetic moment to mass ratio but this also means we are slow-

ing $1/5$ of the atoms in the given 3P_2 metastable state. The efficiencies consider the entire metastable state, meaning an efficiency quoted in Table 3.2, say 2%, is the efficiency of total metastable population. This means if the magnetic projections are equally populated the 2% efficiency quoted corresponds to an efficiency of 10% for the $m_j = 2$ projection. We calculate the efficiency by comparing the area under the curve of the slowed peak to the geometrically scaled area under the reference beam. We normalize to the expected intensity of the reference beam at the entrance of the slower. We do this because the reference beam is taken without the coils on, resulting in added divergence through the slower than what is experienced with the guided slowed peaks.

Since we use a highly efficient detector (the MCP has near unit efficiency) the noise is small compared to molecular oxygen. We cool our nozzle to 77 K and average each data set over 20 shots at a repetition rate of 0.075 Hz. Figures 3.12 and 3.13 show the slowed peaks compared to the main distribution. The plots are shown in two figures for clarity and all the curves besides the main distribution have a vertical offset for ease of comparison. The noise spikes before the slowed peaks are due to the coils, which end about 0.5 ms before the slowed peak arrives at the MCP. The slower peaks select a smaller velocity distribution within the main distribution which is why more of the main distribution remains intact. This is also seen in the slowed peaks, as the velocity of the slowed drops so does the number of atoms in the distribution. The distribution of the final peaks are not uniform due to the anharmonic nature of the potentials created with our coils. This has been investigated by Bethlem *et al.* for the Stark decelerator [25]. The final velocities, temperature, efficiencies, phases are summed up in Table 3.2.

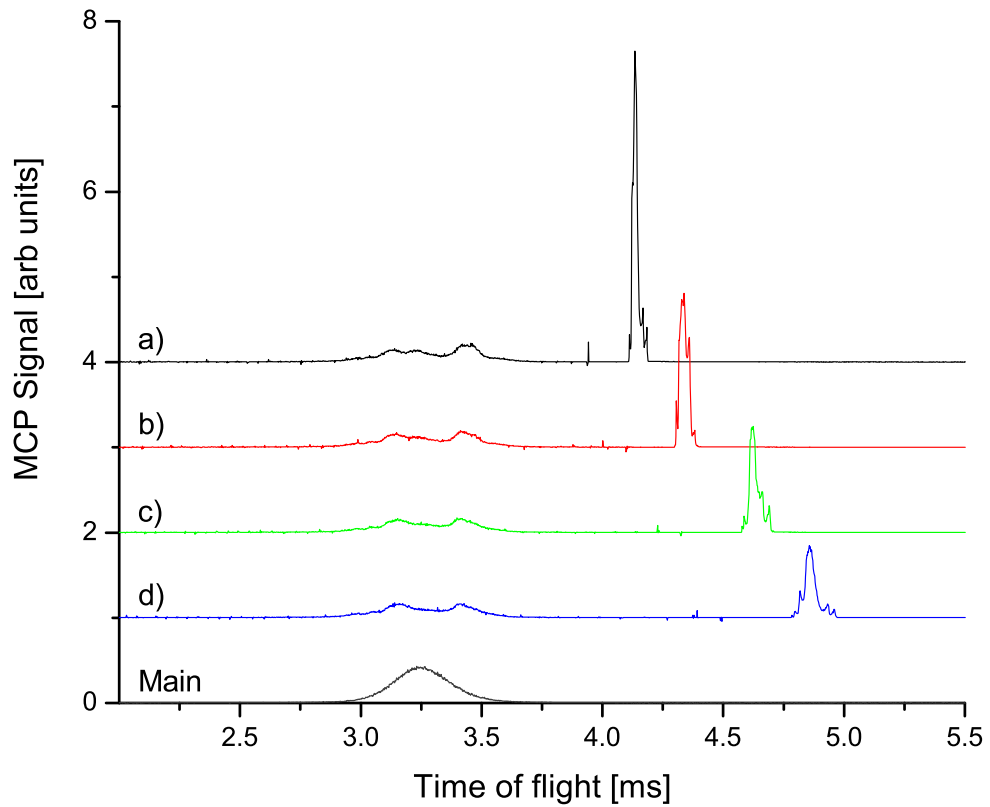


Figure 3.12: Experimental data of slowed metastable neon at different final velocities. These are time of flight measurements taken with a MCP. The main distribution has a velocity of 446.5 m/s. The slowed peaks have velocities of a) 222 m/s, b) 184.7 m/s, c) 142.7 m/s, and d) 109.9 m/s. Each curve represents 20 averages. All the curves besides the main distribution have a vertical offset so they can be compared in one graph.

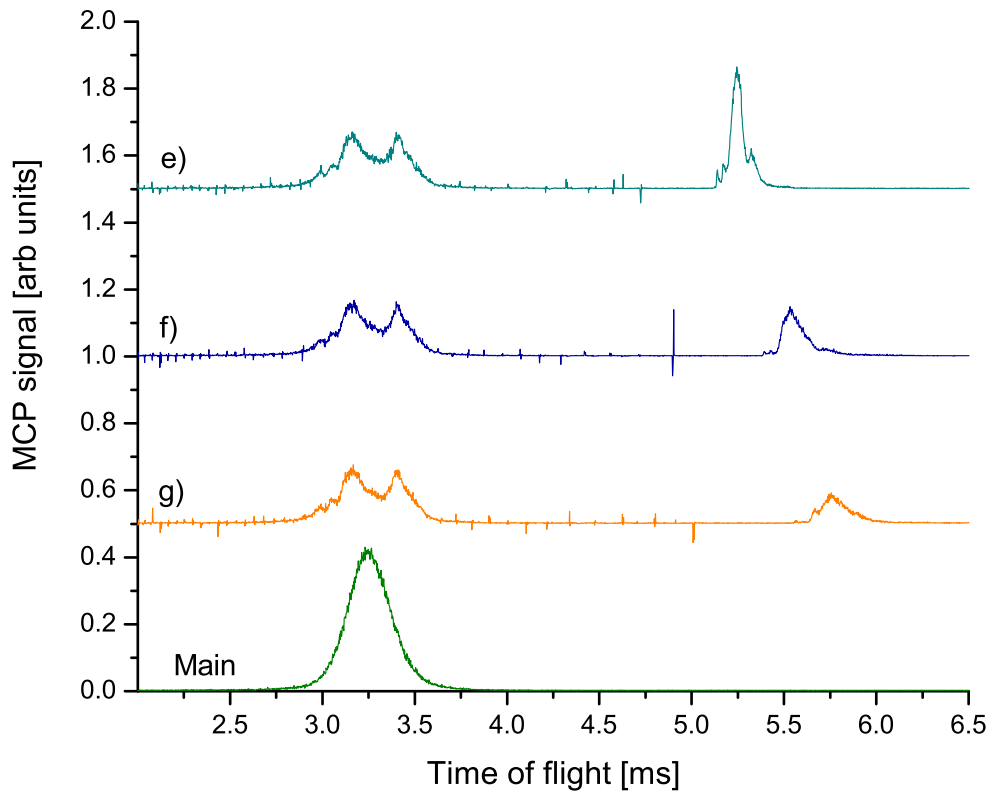


Figure 3.13: Time of flight measurements recorded by a MCP. The main distribution has a velocity of 446.5 m/s. The three slowest peaks have velocities of e) 84.1 m/s, f) 70.3 m/s, and g) 55.8 m/s. Each curve represents 20 averages and all the curves besides the main distribution have a vertical offset for clarity.

Table 3.2: Final velocities [v_f], temperatures [T], efficiencies, and phases for slowed peaks in Figures 3.12 and 3.13

	v_f [m/s]	T [mK]	Efficiency [%]	Phase
Main	446.5 ± 2.5	525 ± 10
a	222 ± 11	108 ± 22	11.9 ± 0.5	37.7°
b	184.7 ± 7.6	184 ± 39	9.6 ± 0.4	39.7°
c	142.7 ± 9.1	117 ± 32	7.2 ± 0.3	41.7°
d	109.9 ± 5.4	147 ± 34	5.5 ± 0.2	42.7°
e	84.1 ± 3.1	79 ± 20	4.1 ± 0.2	43.7°
f	70.3 ± 7.4	92 ± 57	2.9 ± 0.1	44.2°
g	55.8 ± 4.7	106 ± 59	2.0 ± 0.1	44.5°

3.2.2 Molecular Oxygen

Here we show the data for slowed molecular oxygen between phases 47.8° and 63.2° . We use a mixture of oxygen and krypton at a ratio of 1:5 and cool the nozzle to a temperature of 148 ± 1 K to achieve a mean beam velocity of 389 ± 5 m/s. In order to achieve the highest slowing efficiency we tune our slower to slow oxygen in the ground rotational $K = 1$, $J = 2$, $M_j = 2$ sublevel state. Our coils produce high enough magnetic fields to decelerate oxygen to near rest, but are weak enough to avoid level crossings that mix the $K = 1$, $J = 2$, $M_j = 2$ with the $K = 3$, $J = 2$, $M_j = 2$ sublevel which will change the low field seeking atom to a high field seeking atom [26].

Figures 3.14 and 3.15 show the various final velocities over 200 averages at a repetition rate of 0.075 Hz. All the peaks except the main distribution have a vertical offset for clarity and ease of comparison. The signal-to-noise ratio is smaller for oxygen than it is for metastable neon because of the use of the quadrupole mass spectrometer. We slow molecular oxygen from 389 m/s to as low as 83 m/s. Like metastable neon, the slower peaks have fewer atoms due to the

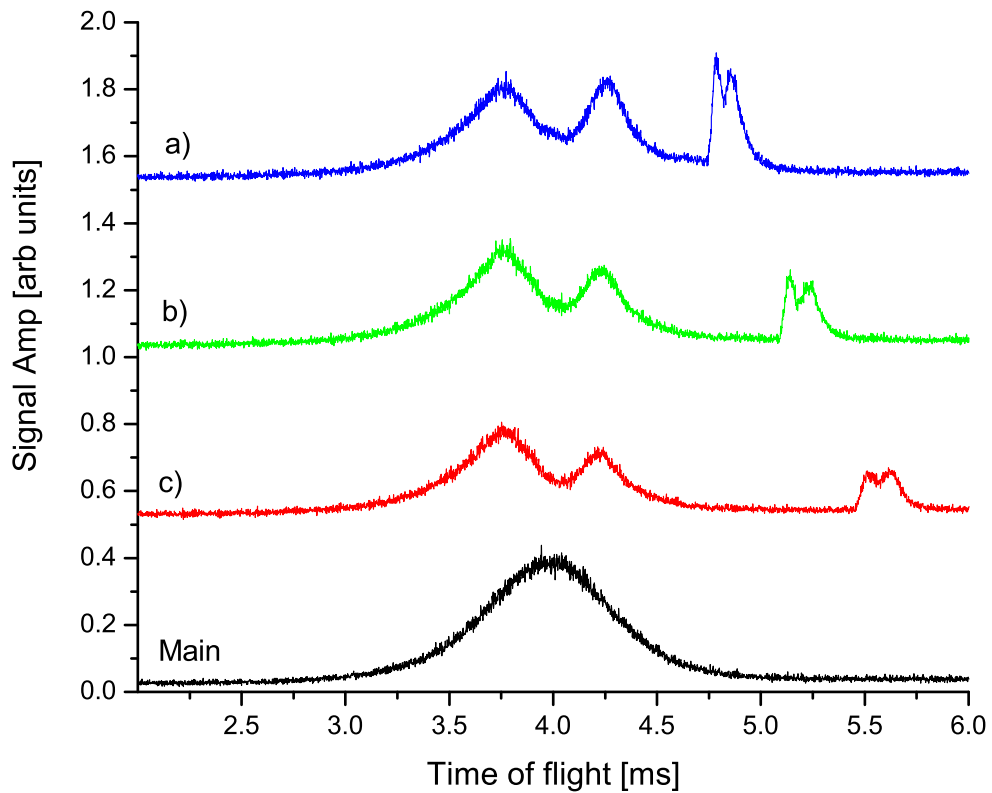


Figure 3.14: Time of flight measurements recorded on a QMS. The main distribution has a velocity of 389 m/s and the slowed peaks have a final velocity of a) 242 m/s, b) 195 m/s, and c) 155 m/s. Each data set is taken over 200 averages at a repetition rate of 0.075 Hz. The peaks have a vertical offset except for the main distribution.

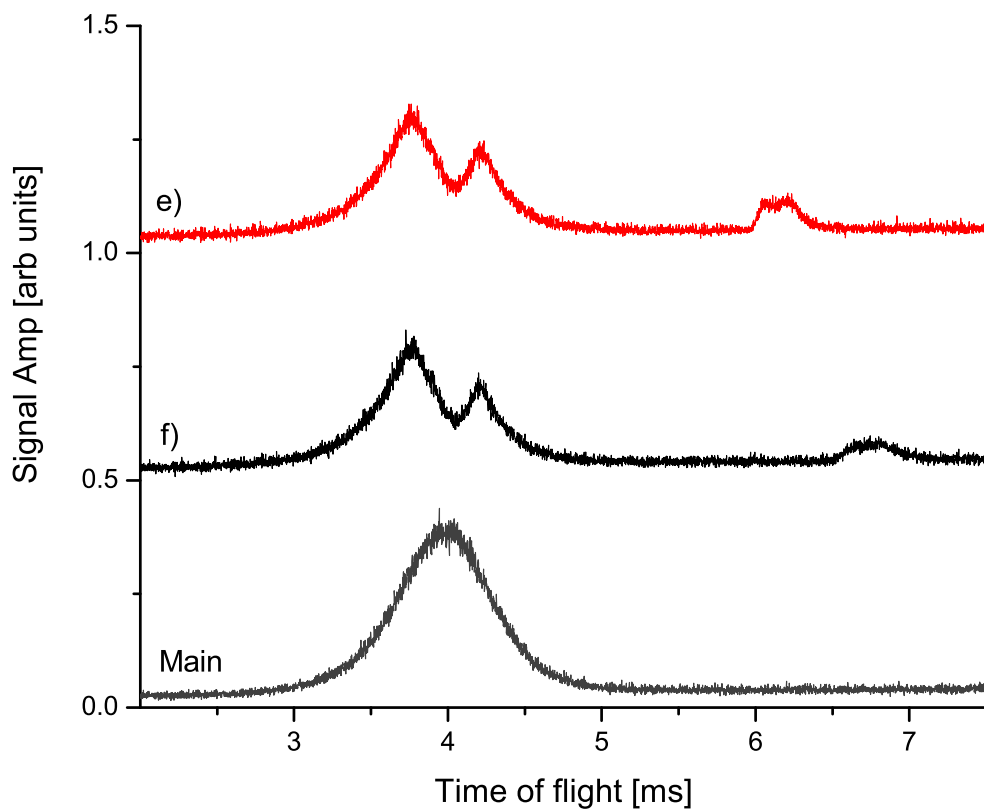


Figure 3.15: Experimental data of slowed molecular oxygen at different final velocities. The peaks corresponds to velocities: main distribution 389 m/s , e) 114 m/s, f) 83 m/s. Each data set is taken over 200 averages at a repetition rate of 0.075 Hz. The slowed peaks have a vertical offset for clarity.

Table 3.3: Final velocities [v_f], ratios, and phase for slowed peaks in Figures 3.14 and 3.15

	v_f [m/s]	ratio [%]	phase
Main	389 ± 5.0
a	242 ± 13	2.3	47.8°
b	195 ± 8	1.7	53.5°
c	155 ± 5	1.2	57.5°
d	114 ± 3	1	61°
e	83 ± 3	0.8	63.2°

phase stability window. A direct comparison of efficiencies could not be directly computed as with metastable neon, due to the uncertainty in ionization in the quadrupole mass spectrometer for the slowed peaks (the ionization probability is different for slower peaks due to the longer interaction time with the detector ionizer). However we did calculate the ratio of area under the slow peak to the geometrically scaled area under the reference beam. The final velocities are summed up in table 3.3.

This is the first demonstration of slowing any supersonic beam of molecules using pulsed electromagnetic coils. This allows slowing and trapping of molecules which have a magnetic moment in the ground state such as molecule radicals or in our case, molecular oxygen.

Chapter 4

Isotope Separation

In this chapter we will discuss a new approach to isotope separation which is more general and efficient than other available methods. First an overview of current technologies will be discussed, and motivation for this new idea will be given. We then explore the generality of our method by discussing two cases: atoms that have non-zero magnetic moment in the ground state and atoms that have zero magnetic moment in the ground state. These two types of atoms make up the entire periodic table. Finally a description of the magnetic guide and simulation results will be given.

4.1 Current Methods

Currently the two biggest methods to producing isotopes commercially are the calutron and centrifuge method. These two methods have been primary used for the bulk of isotopes for nearly 70 years. Figure 4.1 shows which method is used for each isotope.

The centrifuge method is based directly on mass differences between different isotopes [39–41]. The centrifuge contains a fast spinning rotor inside a protective casing. It spins so fast that it pushes heavier atoms to the outside walls and the lighter elements towards the center. Heating the centrifuge will enhance this separation by creating convection currents that further separate the

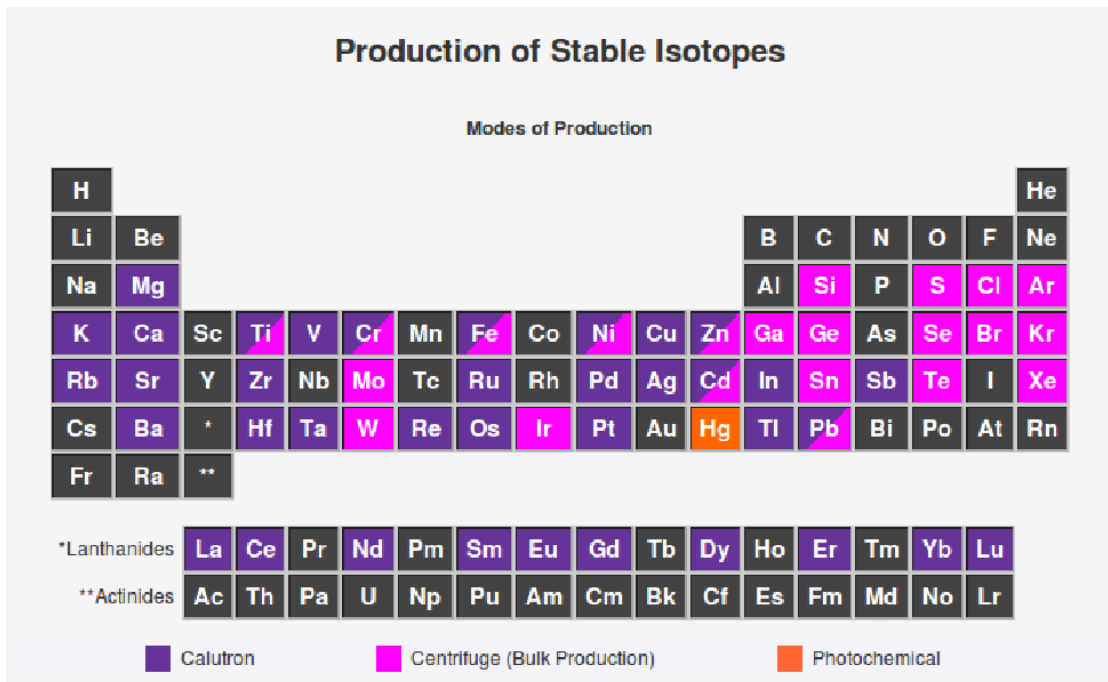


Figure 4.1: This periodic table shows the methods used to separate isotopes of given elements. Most elements are separated with either the calutron or centrifuge method. Courtesy of Trace Sciences.

isotopes. The enrichment factor for each centrifuge is quite low, so many cascades of centrifuges are needed for high enrichment. The centrifuge has long been the method of choice for separation of uranium hexafluoride on large scales, however this method is limited to species which are gaseous at or near room temperature (volatile elements) and cannot separate elements which are solid at room temperature.

The calutron or mass spectrometry is general to all atoms on the periodic table [42, 43] but is very inefficient. This method takes advantage of the fact that every charged particle will follow a certain circular trajectory within a magnetic

field. The radius of this circular trajectory will be different for different isotopes, thus making separation possible. The source of atoms is an oven; as the atoms exit the oven they are ionized and accelerated through the system and are separated. This method is highly selective, and enrichments can be very high. It is inefficient, however, because of the low probability of electron-bombardment ionization, and it is limited by space-charge meaning throughput is low.

In recent years isotope separation using laser ionization has been developed [44]. This process is highly selective but requires multiple high-powered lasers to achieve ionization. This method will only ionize one specific isotope which then can be separated from the rest of the atoms using ion optics. This process works very well but its use of the photons is very inefficient and thus power consumption can be quite large.

4.2 Single-Photon Atomic Sorting

The above techniques have proven valuable over the years. Each have their own drawbacks, however, resulting in a need for a new inexpensive method of producing isotopes. Here we propose a new method of isotope separation called Single-Photon Atomic Sorting, which is very efficient and can be applied to nearly the entire periodic table.

To highlight this new technique I'll first give a general picture of how our method works. We start with an atomic beam of atoms of a single element composed of multiple isotopes. Consider an ideal three level atom with an initial electronic ground state $|i\rangle$, an electronic excited state $|e\rangle$, and a final electronic state $|f\rangle$. We assume the initial magnetic moment m_i is different from the final

magnetic moment m_f . Now assume this atomic beam intersects a laser beam which induces an irreversible transition from $|i\rangle$ to $|f\rangle$ by absorption of the photon followed by spontaneous emission as shown in Figure 4.2. The laser is tuned to only one isotope, changing its magnetic moment but not effecting the other isotopes. Once the transition has been made the beam of atoms enters a magnetic field gradient ∇B , created by a magnetic multiple. The magnetic multiple acts like a guide for the low-field seeking atoms.

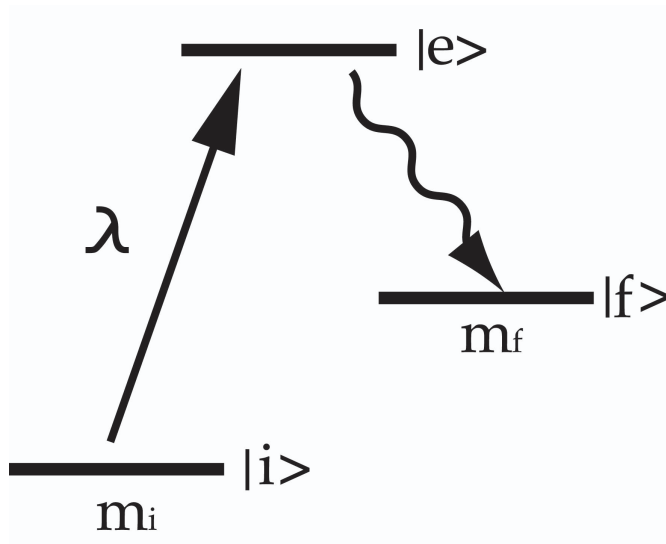


Figure 4.2: The laser beam excites the atom from $|i\rangle$ to $|e\rangle$, and the atom then decays down to $|f\rangle$. The magnetic moments of the initial and final states are different.

In principle the separation of an isotope can be accomplished using only one photon, making the best use of every photon available. The goal is to lower the entropy of the atomic beam by separating the isotopes. In this sense the laser beam acts like a Maxwell's Demon as proposed by Leo Szilard in 1929. This process is very similar to the one-way barrier for atoms that was used to

cool the translational motion of Rb atoms (section 2.3). The atom scatters one photon from the laser, increasing its entropy, but this increase is compensated by the decrease of entropy in the beam. Our method eliminates the need for high powered lasers and uses inexpensive magnets with a supersonic nozzle to produce a scalable and general method for isotope separation.

4.2.1 Entrainment

Many elements are solid at room temperature and can not be directly put into a supersonic nozzle. To apply our method to the entire periodic table, we must entrain a species of atoms into a supersonic flow. We do this experimentally by putting an oven close to the aperture of the nozzle as shown in Figure 4.3. The top and bottom of the oven are held at different temperatures, forming a gradient which creates a collimated effusive beam over the region intersected by the supersonic beam. The inside of the oven is lined with a stainless steel mesh which wicks back atoms which are not entrained in the supersonic beam. The oven is self-circulating in the sense that atoms not entrained are contained in the oven and will have another chance to be entrained. This oven is very similar to continuous reflux ovens [11]. In order to simulate the entrainment achievable with such an oven, we used the Direct Simulation Monte Carlo method created by Professor Graeme Bird from the University of Sydney in Australia [45]. This method is widely used to simulate rarified gas dynamics like those present in supersonic beams. The simulations shown here are provided by Professor Uzi Even from the Sackler School of Chemistry, Tel-Aviv University. The simulation assumes the temperature of the lithium to be 900 K at a pressure of 1 pascal, and the oven is placed 1 cm away from the supersonic nozzle. Figure 4.4 shows

entrainment of lithium into a neon supersonic carrier gas at an efficiency of 10%.

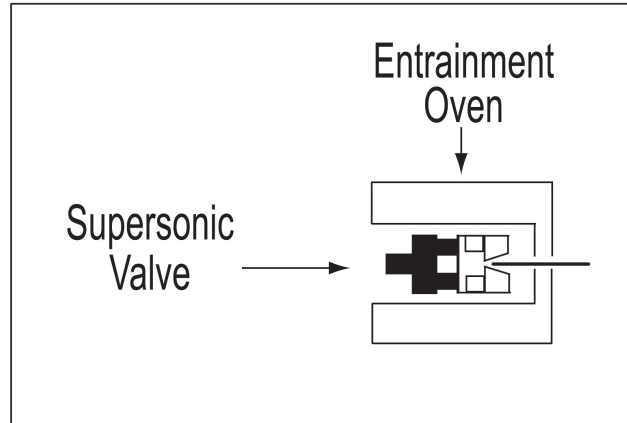


Figure 4.3: Schematic of the supersonic valve and entrainment oven.

Figure 4.5 shows the temperature of the supersonic beam. The graph shows heating of the beam to about 200 K, but then the supersonic beam continues to cool as it expands through the entrainment region. This cooling happens because the beam is still collisional and still expanding well past the oven region. The atoms entrained take on the characteristics of the supersonic beam, namely low velocity spread and very low divergence. Producing a high flux atomic beam is the first step in the ability to scale up this technique.

4.2.2 Magnetic Guiding

Once we have a high flux atomic beam, we use a laser to change the isotope of choice into a low-field seeking atom. We want this magnetic state because we use a magnetic quadrupole or hexapole to guide the low-field seeking atoms. Both of these guides produce a magnetic field minimum in the center that forces low-field

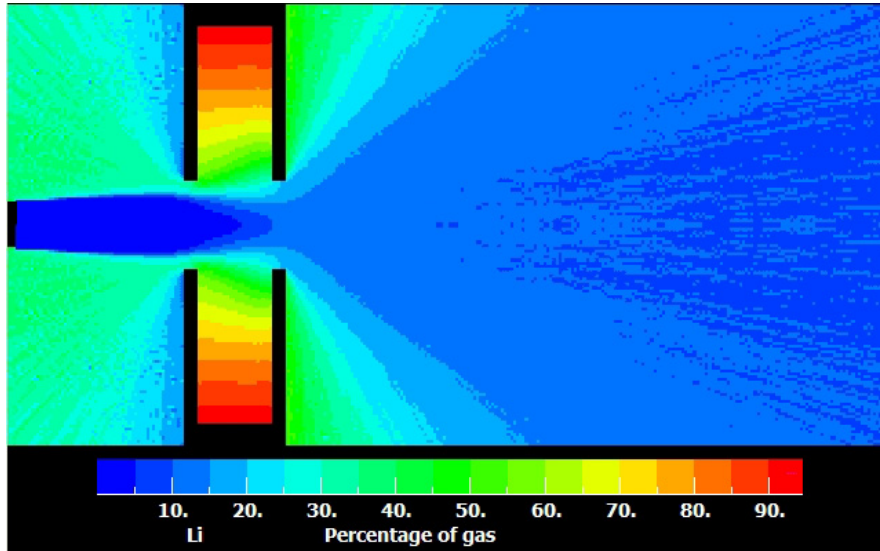


Figure 4.4: Direct Monte Carlo simulation of entrainment of lithium into a neon supersonic gas. It shows entrainment efficiencies at 10%, which make large scale separation feasible. Figure is from Professor Uzi Even at the Sackler School of Chemistry, Tel-Aviv University.

seeking atoms to be guided towards the center of the magnetic guide. High-field seeking states get pushed to regions of high magnetic field and will ultimately collide with the inside of the guide where they will stick to the walls.

We show here two types of magnetic guides, both with their own advantages. We simulate both guides using 12.7 x 12.7 x 25.4 mm magnets with a residual flux density of $B_r = 1.48$ T. These magnets are very strong and inexpensive which eliminates the need for superconducting magnets. The design we use for both guides is similar to those used for guiding a neutral beam of atoms [46, 47].

The quadrupole is composed of four permanent magnets. Figure 4.6 shows the finite element analysis for a quadrupole magnetic field where the arrow shows

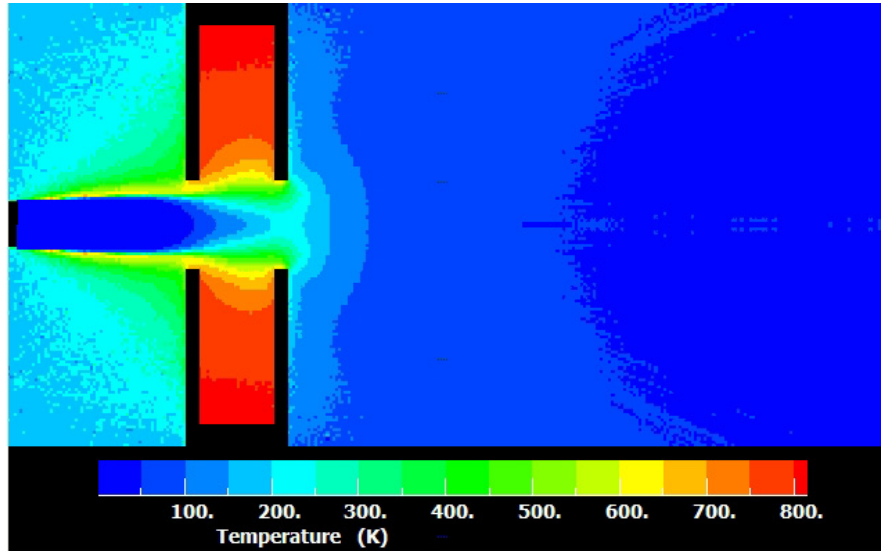


Figure 4.5: A temperature map of lithium entrained into a neon supersonic beam. The supersonic beam heats up in the oven but cool down after the oven. Figure is from Professor Uzi Even at the Sackler School of Chemistry, Tel-Aviv University

the magnetization direction. The magnets surround a 1.5 cm inner diameter (1.6 cm outer diameter) stainless steel tube. The inside of the tube will be in vacuum, while the magnets will be held outside of vacuum. The advantage of the quadrupole is its small size tube and strong gradients. We find this guide useful for separation of lighter atoms like lithium. Reducing the size of the guide will result in larger gradients but will reduce the amount of collected atoms, cutting down throughput.

The hexapole is composed of six permanent magnets orientated as shown in Figure 4.7. Figure 4.7 shows the finite element analysis for a hexapole field. Both the hexapole and quadrupole fields are simulated using COMSOL Multiphysics. The six magnets surround a 2.12 cm inner diameter (2.22 cm outer diameter)

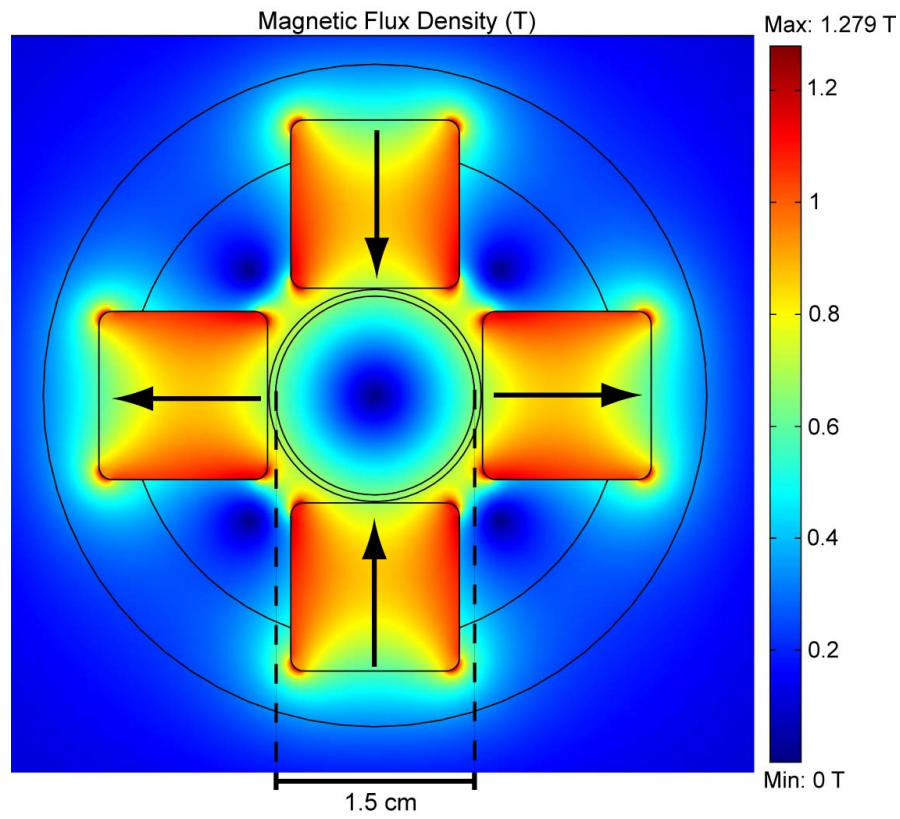


Figure 4.6: The magnetic flux density of a quadrupole field produced by four permanent magnets. The magnets surround a 1.5 cm inner diameter (1.6 cm outer diameter) stainless steel tube. The magnets are held in place with an aluminum holder. The inside of the tube is vacuum, and the magnets are held outside vacuum. The arrows denote the direction of magnetization for each magnet.

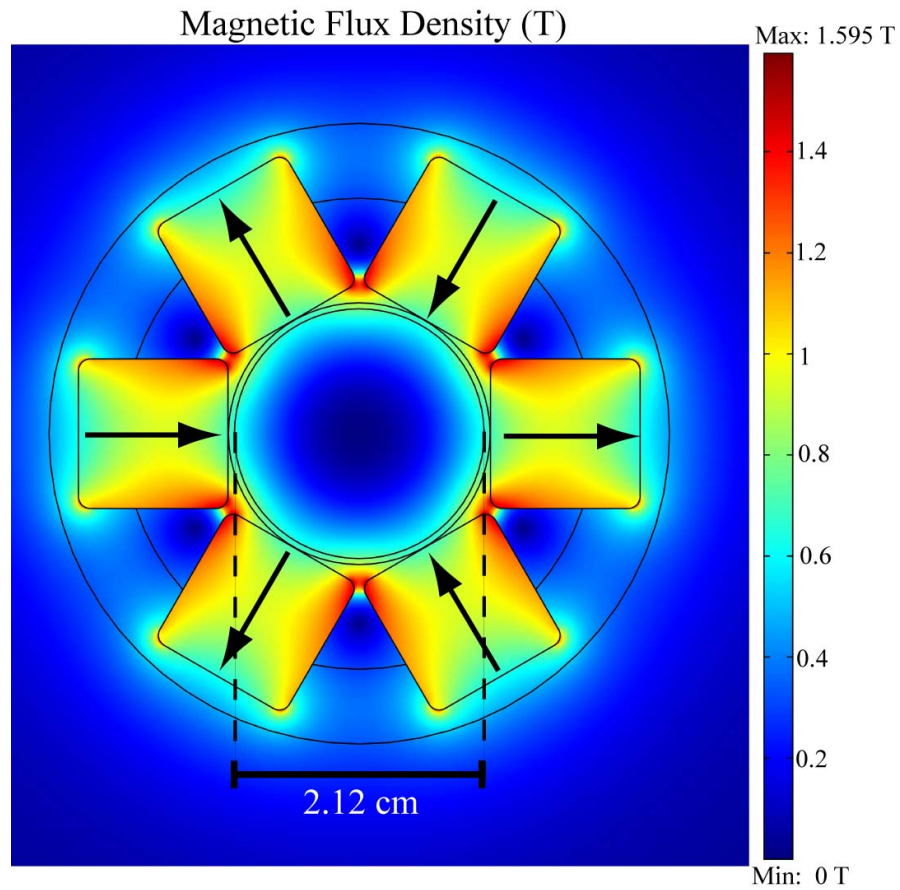


Figure 4.7: The magnetic flux density of a hexapole field. The magnets surround a 2.12 cm inner diameter (2.22 cm outer diameter) stainless steel tube. The magnets are held by an aluminum holder out of vacuum. The arrows denote the direction of the magnetization for each magnet.

stainless steel tube. This configuration is held together with an aluminum holder. The advantages of the hexapole are the larger diameter and acceptance angle of the incoming atoms. The disadvantage is the lower gradients, meaning a longer guide will be needed with this design. We found that a hexapole guide is better for heavier atoms because of the added acceptance angle for larger throughput.

We export from our finite element analysis a 500 x 500 array giving the magnetic field values at each point. The simulation then extrapolates between points creating a complete 2D profile of the magnetic guide. We do this instead of using equation 2.25 since an analytical expression requires higher order corrections to account for geometry [27].

4.2.3 Non-Zero Magnetic Moment in Ground State

We now discuss an example of an atom that has a non-zero magnetic moment in the ground state. Most atoms have a magnetic moment in the ground state, and we will focus on the separation of ${}^6\text{Li}$ and ${}^{150}\text{Nd}$ while highlighting the technique's general applicability. ${}^6\text{Li}$ is considered because of its ease of separation, and ${}^{150}\text{Nd}$ is chosen due its double beta decay that is used to investigate the Dirac or Majorana nature of the neutrino. These examples show how our method can be adapted to both low and high mass species.

4.2.3.1 Lithium

Figure 4.8 shows the experimental overview of the separation of ${}^6\text{Li}$. Lithium is an easy case because it only has two isotopes, ${}^6\text{Li}$ and ${}^7\text{Li}$ with natural abundances of 7.6% and 92.4%, respectively. In this case a single laser will be tuned to the ${}^7\text{Li}$ D₂-line ($2^2\text{S}_{1/2}(\text{F}=2) \rightarrow 2^2\text{P}_{3/2}(\text{F}=1 \text{ or } \text{F}=2)$), which will optically pump

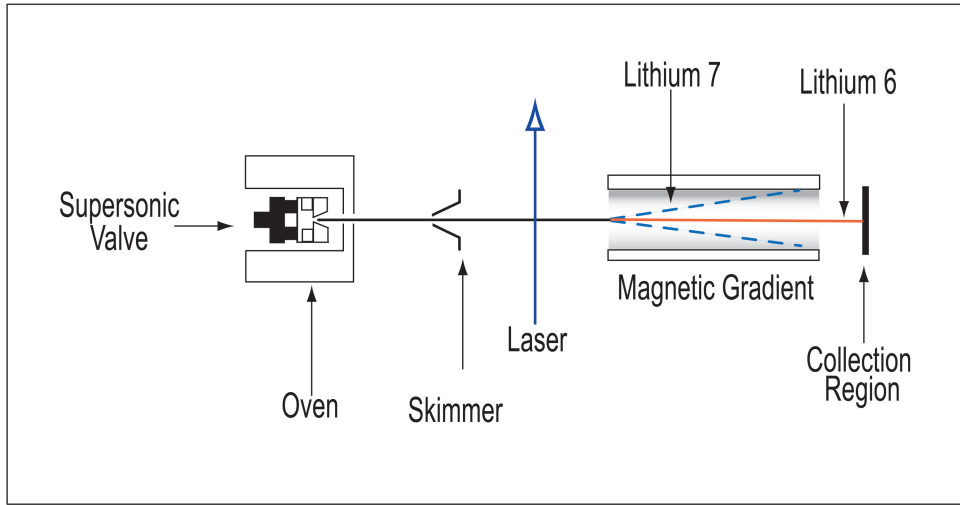


Figure 4.8: Schematic of Single-Photon Atomic Sorting. The oven crosses the supersonic beam, which uses an inert carrier gas such as a noble gas. The laser intersects the beam, and the unwanted isotopes are filtered by the multipole magnetic guide.

all of the ${}^7\text{Li}$ atoms into the ${}^2\text{S}_{1/2}$ $F=2$ manifold. At fields greater than 50 G the entire $F = 1$ manifold will become high-field seeking, causing ${}^7\text{Li}$ to be anti-guided within the magnetic quadrupole. Since we do not touch the ${}^6\text{Li}$ with a laser we will take a statistical loss of one half of the ${}^6\text{Li}$ because of the magnetic sub-level projections. Figure 4.9 shows the length of quadrupole needed for most of the ${}^7\text{Li}$ atoms to collide and stick to the walls of the quadrupole guide. We find that the bulk of the ${}^7\text{Li}$ hit the walls between 10 to 30 cm upon entering the guiding tube. After 50 cm we see that very little ${}^7\text{Li}$ will hit the walls, so the simulation uses a 50 cm long magnetic guide.

Figure 4.10 shows the radial distributions of the two lithium isotopes entering the magnetic region, as well as their distributions upon exiting the magnetic

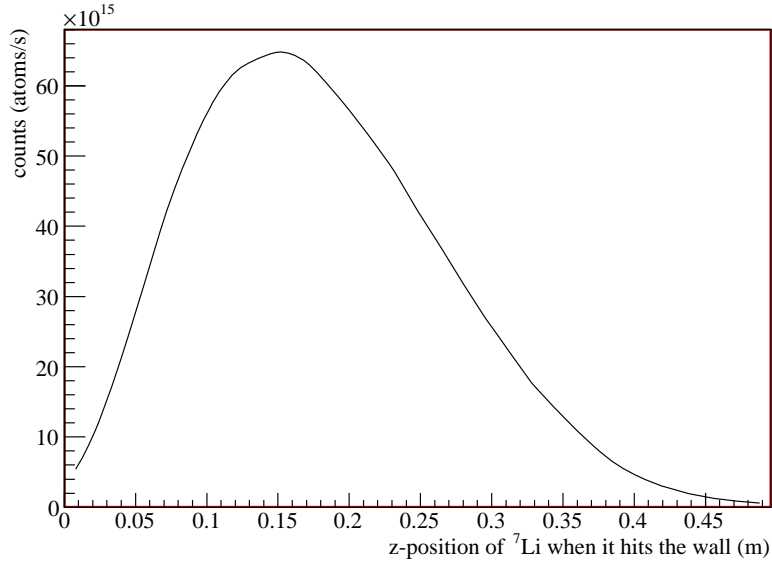


Figure 4.9: This plot shows the when the anti-guided ${}^7\text{Li}$ atom hit the walls in counts/sec. This was simulated using the quadrupole field in Figure 4.6. The number of atoms hitting the wall after 45 cm is near zero thus a 50 cm long quadrupole guide is enough to sufficiently filter out almost all of the ${}^7\text{Li}$.

guide. The simulation assumes a supersonic beam with a mean velocity of 800 m/s and an initial Gaussian spread of 15 m/s in each component of the beam velocity. Figure 4.10 shows a 95% enrichment of ${}^6\text{Li}$ and 36.8% of the ${}^6\text{Li}$ is collected. The percentages quoted here and in Table 4.1 represent the percentage of atoms that make it to end of the magnetic guide given that they survive the skimmer. The Even-Lavie valve has a flux of 4×10^{23} atoms/s/sr, but given that the nozzle is pulsed at 1 kHz, and given available pumping speeds, the continuous beam flux would be $\sim 5 \times 10^{22}$ atoms/s/sr. We intend to place a 5 mm diameter skimmer 15 cm from the nozzle which implies a flux of $\sim 3 \times 10^{18}$ atoms/s, and at 10% entrainment the flux of lithium atoms that survive the skimmer is ~ 3

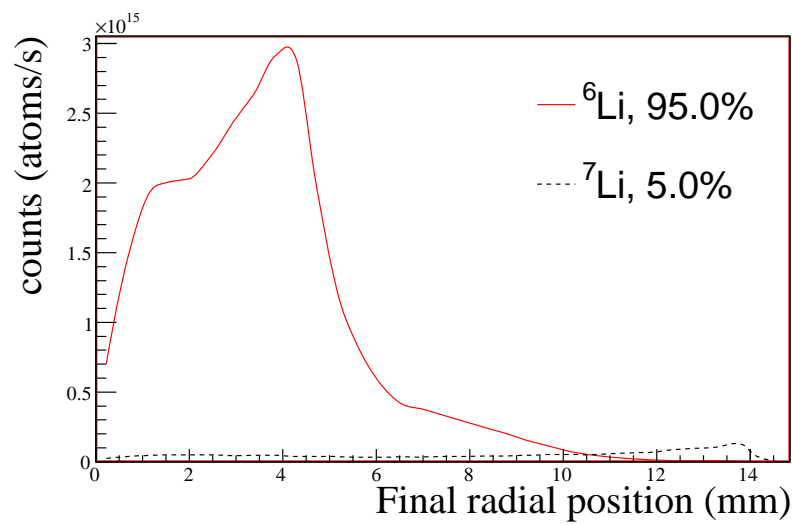
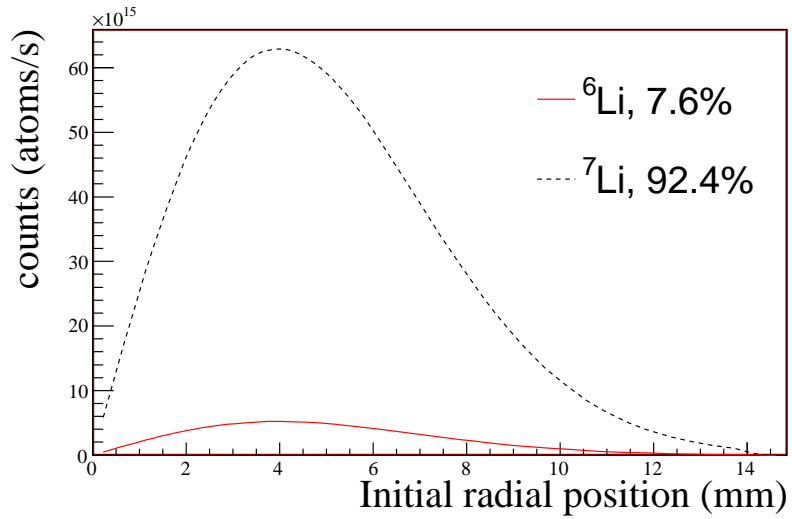


Figure 4.10: The radial positions of ^6Li and ^7Li atoms before entering the quadrupole guide and after. You see ^7Li is nearly depleted at the exit. This shows an enrichment of ^6Li to 95%.

$\times 10^{17}$ atoms/s. If 36.8% makes it through the magnetic guide and the natural abundance of ${}^6\text{Li}$ is 7.6%, we expect our throughput to be $\sim 8 \times 10^{15}$ atoms/s.

All simulations of the radial distributions are programmed in ROOT. ROOT is a C++ based object-oriented program and library developed and maintained by CERN.

4.2.3.2 Neodymium

Neodymium is a tougher case because it has 7 stable isotopes and is very heavy compared to lithium. We therefore simulate neodymium using a hexapole, which helps collect a larger amount of atoms as compared to the quadrupole. To gain the highest efficiency we must also optically pump neodymium with a polarized laser beam (σ^+ and σ^-). We want to pump ${}^{150}\text{Nd}$ to the low-field seeking stretch state and pump all other isotopes into the high-field seeking stretch state (The “stretch state” refers the state in which m_j has the largest possible magnitude). We do this because we can get the greatest separation power. While optical pumping does mean that more than one photon has to be scattered, only a small number of photons is needed, meaning this method still makes extremely efficient use of laser power. While scattering only one photon makes separation possible, optical pumping will be needed to reach high enrichments for many elements.

Neodymium has a ground state of ${}^5\text{I}_4$. We can optically pump the ground state to a $J' = 4$ excited state with a 471.9 nm laser [48]. This transition has favorable branching ratios, and the simulation results in Figure 4.11 take them into account. The simulation assumes a beam with a mean velocity of 500 m/s and

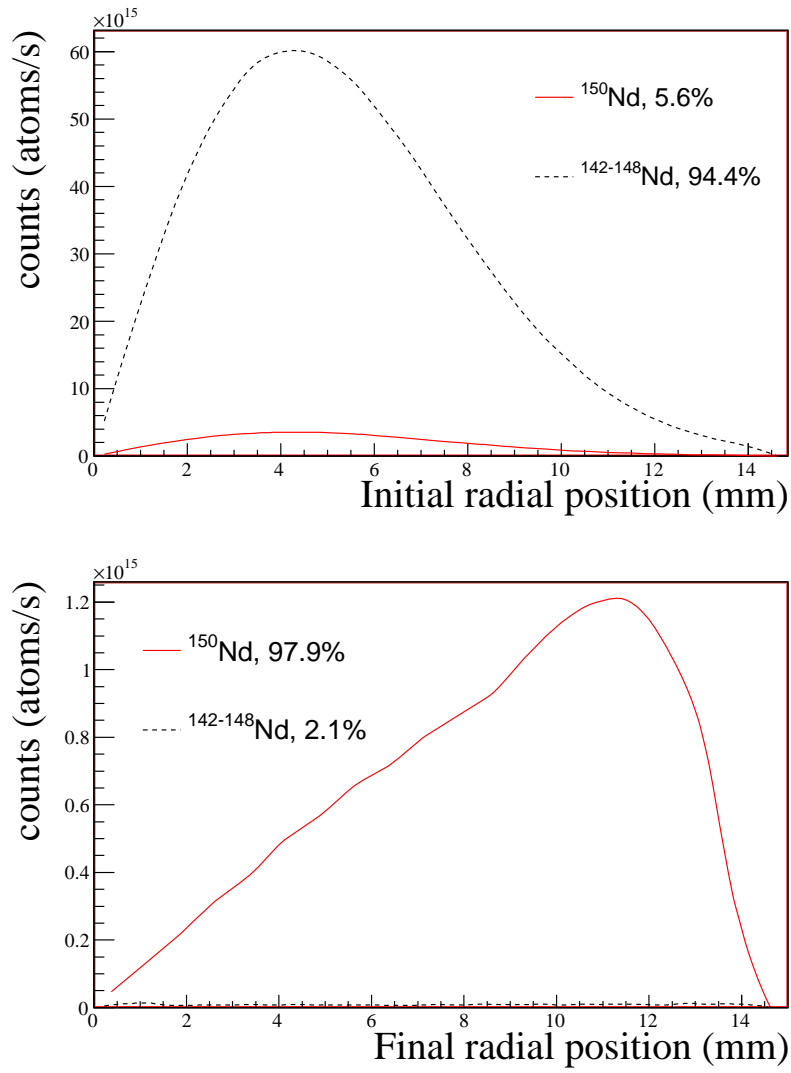


Figure 4.11: The radial positions of neodymium isotopes as they enter the hexapole magnetic guide followed by their radial positions upon exiting. ^{150}Nd is enriched to 97.9%.

a Gaussian spread of 15 m/s in each component of the supersonic beam velocity. Since neodymium is heavier than lithium, it can be seeded into a heavier carrier gas that has a lower mean beam velocity. The simulation uses a 2 m long hexapole magnetic guide. Figure 4.11 shows the radial distribution of ^{150}Nd along with the other isotopes. The simulation shows enrichment of ^{150}Nd to 97.9% and collection of 23.0% ^{150}Nd that survives the skimmer. At 10% entrainment, 5.6% natural abundance, and 23.0% collection we expect a throughput of $\sim 4 \times 10^{15}$ atoms/s.

4.2.4 Zero Magnetic Moment in Ground State

A small class of atoms have a zero magnetic moment in the ground state. In order to separate these atoms we must promote the desired isotope into a suitable metastable state which does have a magnetic moment. Most atoms with a zero magnetic moment in the ground state do have a suitable metastable state which does have a magnetic moment. We show the example of separation of ^{44}Ca , because calcium isotopes are widely used in the medical industry.

4.2.4.1 Calcium

Since we are only exciting the isotope of choice to a metastable state, the other isotopes remain in a zero-magnetic moment state. A zero magnetic state means they will not be affected by the magnetic fields and will fly right through the magnetic gradient untouched. We do not want those isotopes to reach the end of the tube, so we bend our magnetic guide to eliminate the line of sight to the collection region. This bend eliminates the unwanted isotopes. Bending a magnetic guide has been done experimentally to guide a beam of metastable neon [46, 47]. Figure 4.12 shows a schematic of the bent magnetic guide.

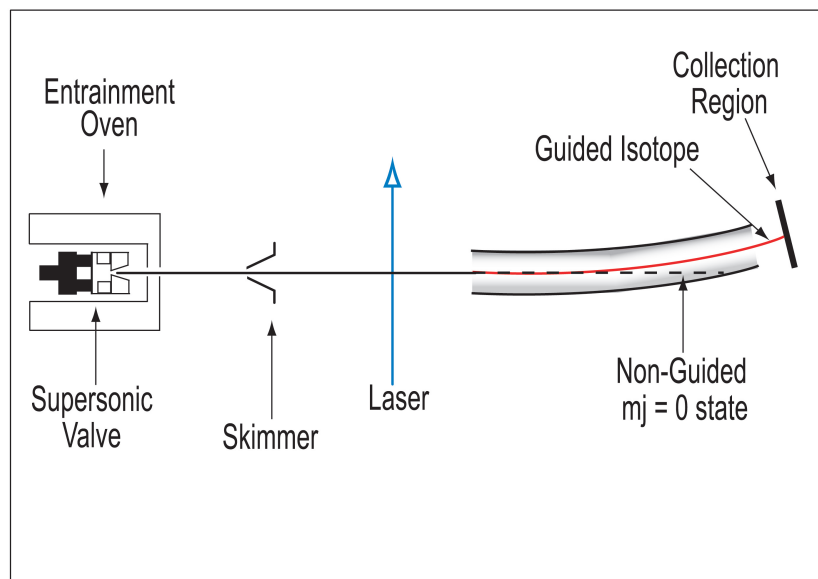


Figure 4.12: Schematic of Single-Photon Atomic Sorting applied to elements which have zero magnetic moment in the ground state. The laser promotes the isotope of choice into a metastable state, and it is guided through the magnetic filter. The magnetic guide is bent to ensure unwanted isotopes hit the wall of the guide before reaching the collection region.

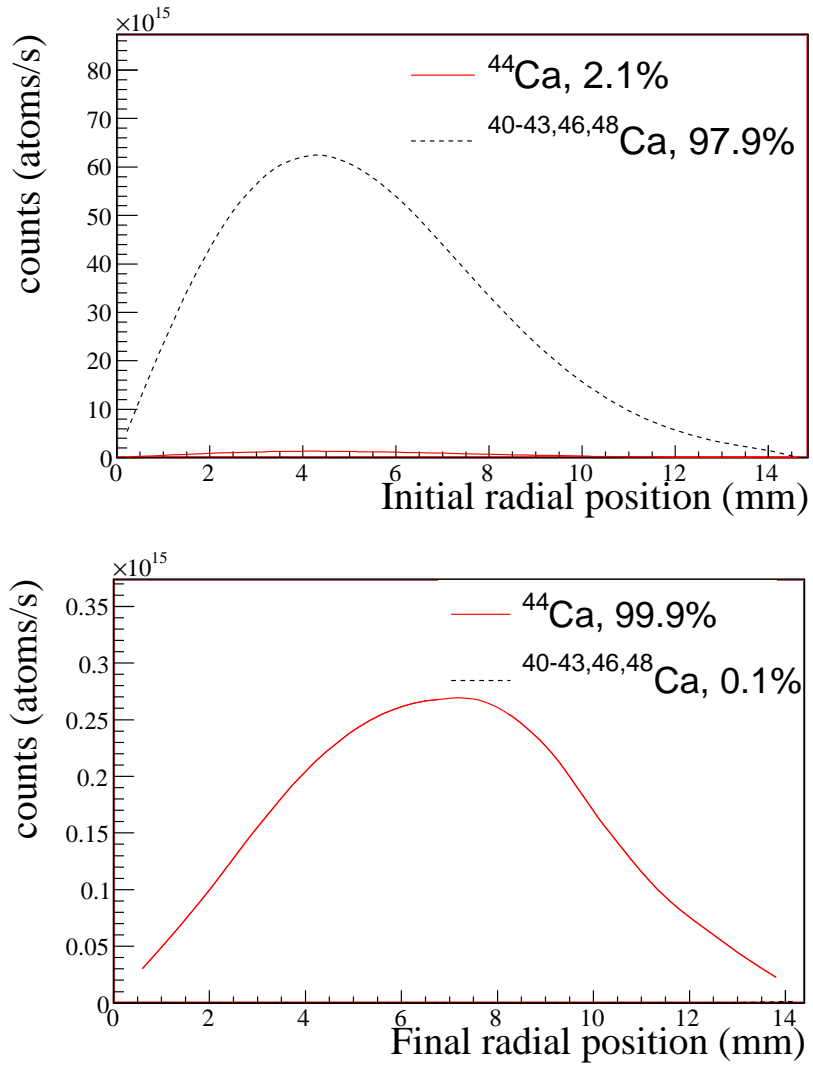


Figure 4.13: The radial distributions of calcium before and after the magnetic guide. We collect 9.0% of ^{44}Ca that survives the skimmer at 99.9% purity.

Table 4.1: Simulation results of Single-Photon Atomic Sorting.

Target Isotope	Natural Abundance	Laser λ [nm]	Enrichment	Collected Isotope	Throughput $\times 10^{15}$ [atoms/s]
${}^6\text{Li}$	7.6%	670.96	95.0%	36.8%	8
${}^{44}\text{Ca}$	2.1%	272.2	99.9%	9.0%	0.6
${}^{150}\text{Nd}$	5.6%	471.9	97.9%	23.0%	4

Using a 272.2 nm laser we can excite ${}^{44}\text{Ca}$ to the ${}^1\text{P}_1^0$ excited state, which decays to both the ground state and to the ${}^1\text{D}_2$ metastable state. A few photons will need to be scattered, but the laser power is still being used very efficiently. Figure 4.13 shows the radial distribution for ${}^{44}\text{Ca}$. This simulation assumes a initial beam velocity of 500 m/s and a Gaussian spread of 15 m/s in each component of the supersonic beam velocity. The magnetic guide is 2 m long with a 6 cm bend over the entire length. We can collect 9.0% of the ${}^{44}\text{Ca}$ at 99.9% purity. At a natural abundance of 2.1%, we estimate our throughput to be $\sim 6 \times 10^{14}$ atoms/s.

The simulation results for all the cases are shown in Table 4.1. The throughput quoted shows numbers which are attainable given current pumping speeds and with 10% entrainment into the supersonic beam. The throughput is orders of magnitude higher than any effusive atomic beam produced in an oven [49].

Chapter 5

Conclusion

In this thesis I presented general techniques to manipulate and control atoms by their magnetic moments. Magnetic moments are universal to all atoms on the periodic table either in the ground state or metastable state, making magnetic slowing and isotope separation possible for all these atoms.

5.1 Magnetic Slower

We have experimentally demonstrated slowing of metastable neon from 446.5 ± 2.4 m/s to as low as 55.8 ± 4.7 m/s and molecular oxygen from 389 ± 5 m/s to as low as 83 ± 3 m/s using a 64 stage coilgun. Efficiencies for neon are as high as $11.9 \pm 0.5\%$, but this percentage depends on the phase used. Our technique can be applied to the slowing and trapping of tritium, which has never been trapped. Tritium is of special interest for its bound state decay which has never been observed experimentally, and for its low endpoint energy. Trapping and cooling tritium could enable a new type of tritium beta decay experiment to measure the absolute mass scale of the neutrino [50].

Also, slowing and trapping of molecules is particularly important for cold chemistry. Currently, trapped molecules are cooled down to hundreds of millikelvin using techniques like buffer gas cooling. To reach lower temperatures requires a different method. Applying Single-Photon Cooling to molecules could

potentially cool molecules further and will allow experimental studies of ultra cold reactions [51]. The magnetic slower and Single-Photon Molecular Cooling used in tandem will be able to slow, trap, and cool molecules to temperatures beyond current limits.

5.2 Isotope Separation

We have shown simulation results of Single-Photon Atomic Sorting applied to two different cases of atoms, one with magnetic moment in the ground state, and the second with a zero magnetic moment in the ground state. Both of these cases are possible to separate with our technique. Isotopes have long been valuable for basic research, defense, nuclear energy, and medicine.

One isotope of interest for basic research is ^{150}Nd which is a double-beta decay emitter. The SNO+ collaboration is in need of ~ 50 kg of ^{150}Nd for their experiment. Providing the SNO+ collaboration with enriched ^{150}Nd will significantly increase their sensitivity to the half life of the double beta decay of ^{150}Nd . Although our throughput of 4×10^{15} atoms/s is not enough to provide the 50 kg needed, one can easily build multiple separators for this purpose. Scalability of our method is not like that of the centrifuge which needs many setups in a cascade, each separator with our method is completely independent. Since our method uses photons efficiently one high power laser can run multiple separators simultaneously.

Many types of isotopes are used in medical research like ^{33}S , which could be use in neutron irradiation. ^{33}S could potentially be a better isotope than ^{10}B in killing tumoral cells [52]. Currently, ^{10}B remains the isotope of choice for

neutron irradiation because it can be separated cheaply, but concerns of toxicity have scientists looking for alternatives like ^{33}S . Also many isotopes of calcium are used extensively in clinical research and nutritional studies. Calcium isotopes are extremely important, but also, extremely expensive. If the price of both ^{33}S and calcium isotopes can be brought down, these isotopes could be used extensively in clinical testing.

Appendix A

Spectroscopic Notation

A.1 Atoms

The common notation used in this thesis as well as in atomic physics is as follows

$$^{2S+1}L_J$$

where the $2S+1$ designates the spin multiplicity, L is the total orbital angular momentum, and J is the total electron angular momentum of the atom. We use letters to denote the value of L in place of numbers

$$L = 0 \rightarrow \text{S}$$

$$L = 1 \rightarrow \text{P}$$

$$L = 2 \rightarrow \text{D}$$

$$L = 3 \rightarrow \text{F}$$

$$L = 4 \rightarrow \text{G}$$

and so on. The letters go in alphabetical order but skip over the letter J . For example, the atomic state $S = 1$, $L = 1$, $J = 2$ is denoted as $^3\text{P}_2$

A.2 Diatomic Molecules

In analogy to atoms, diatomic molecules also have spectroscopic notation. In molecules the total orbital angular momentum of the electrons is not conserved because of the interaction between the nuclei and the motion of the electrons [53].

Diatomic molecules do however possess axial symmetry passing through the two nuclei. This means the projection of the electrons' orbital angular momentum onto the molecular axis is conserved. The absolute value of this projection is denoted as Λ . Like L , Λ is denoted by Greek letters not numbers

$$\Lambda = 0 \rightarrow \Sigma$$

$$\Lambda = 1 \rightarrow \Pi$$

$$\Lambda = 2 \rightarrow \Delta$$

$$\Lambda = 3 \rightarrow \Phi$$

and so on. Since Λ only determines the magnitude of this projection, it does not tell us the sign of the projection. If by reflecting the molecule through the plane passing through the molecular axis twice, the sign of the wavefunction can change. Molecular states that change sign under this reflection are denoted with a -, likewise states that do not change sign are denoted with +. Also it is useful to include the projection of the total electronic angular momentum on the internuclear axis, which is denoted as Ω (Ω is the equivalent of J). The notation is as follows

$$^{2S+1}\Lambda_{\Omega}^{+/-}$$

Finally, one must consider symmetry around the center of mass. If the molecule's nuclei are identical (homonuclear) then the molecule is symmetric around the center of mass. This means if we transform the positions of the electrons from $\vec{r} \rightarrow -\vec{r}$ the square of the wavefunction should be invariant. This means the wavefunction can change sign while the square of the wavefunction remains unchanged. Wavefunctions that change sign are denoted with u and wavefunctions which do not change sign are denoted with g . The letters come from German *ungerade* and *gerade*, which mean odd and even, respectively. This symmetry is denoted with an additional subscript and the complete spectroscopic notation for

a diatomic molecule is,

$${}^{2S+1}\Lambda_{\Omega,g/u}^{+/-}$$

For example, molecular oxygen in the triplet ground state is: $\Lambda = 0$, $S = 1$, $K = 1$, $\Omega = J = 2$, ($J = S + L + K$, but for $\Lambda = 0$, $L = 0$) so the full notation is denoted as: ${}^3\Sigma_{2,g}^-$

Bibliography

- [1] O. Stern, and W. Gerlach. Der experimentelle Nachweiss der Richtungsquantelung im Magnetfeld. *Zeits. Phys.*, **9**, 349 (1922).
- [2] H. J. Metcalf and P. Van der Straten. *Laser cooling and trapping*. Springer-Verlag New York, Inc., (1999).
- [3] K. B. Davis *et al.* Bose-Einstein Condensation in a Gas of Sodium Atoms. *Phys. Rev. Lett.*, **75**, 22 (1995).
- [4] M. H. Anderson, J. R. Ensher, M. R. Matthews, C. E Wieman, and E. A. Cornell. Observation of Bose-Einstein Condensation in a Dilute Atomic Vapor. *Science*, **269**, 198 (1995).
- [5] J. M Doyle, B. Friedrich, J. Kim, and D. Patterson. Buffer-gas loading of atoms and molecules into a magnetic trap. *Phys. Rev. A*, **52**, 2515 (1995).
- [6] M. F. Reidel. *Elastic slowing of a supersonic beam*. The University of Texas at Austin, Master Thesis (2006).
- [7] E. Narevicius *el al.* Coherent slowing of a supersonic beam with an atomic paddle. *Phys. Rev. Lett.*, **98**, 103201 (2007).
- [8] M. Gupta and D. Herschbach. Slowing and Speeding Molecular Beams of Means of a Rapidly Rotating Source. *J. Phys. Chem. A*, **105**, 1626 (2001).

- [9] U. Even, M. Hillenkamp, and S. Keinan. Condensation limited cooling in supersonic expansions. *J. Chem. Phys.*, **118**, 8699 (2003).
- [10] H. Pauly. *Atom, Molecule, and Cluster Beams*. Springer Berlin; New York, Vol **1**, (2000).
- [11] R. D. Swennumson and U. Even. Continuous flow reflux oven as the source of an effusive molecular Cs beam. *Rev. Sci. Instrum.*, **52**, 4 (1981).
- [12] F. B. Dunning and R. G. Hulet. *Atomic, Molecular, and Optical Physics: Atoms and Molecules*. Academic Press, Vol **29B**, (1996).
- [13] E. Narevicius *et al.* Stopping supersonic beams with a series of pulsed electromagnetic coils: an atomic coilgun. *Phys. Rev. Lett.*, **100**, 093003 (2008).
- [14] E. Narevicius *et al.* An atomic coilgun: Using pulsed magnetic fields to slow a supersonic beam. *New J. Phys.*, **9**, 358 (2007).
- [15] E. Narevicius *et al.* Stopping supersonic oxygen with a series of pulsed electromagnetic coils: a molecular coilgun. *Phys. Rev. A*, **77**, 051401 (2008).
- [16] G. N. Price, S. T. Bannerman, K. Viering, E. Narevicius, and M. G. Raizen. Single-Photon Atomic Cooling. *Phys. Rev. Lett.*, **100**, 093004 (2008).
- [17] S. T. Bannerman, G. N. Price, K. Viering, and M. G. Raizen. Single-photon cooling at the limit of trap dynamics: Maxwell's demon near maximum efficiency. *New J. of Phys.*, **11**, 063044 (2009).

- [18] G. N. Price. *Single-Photon Atomic Cooling*. PhD thesis, University of Texas at Austin, (2009).
- [19] M. Jerkins, I. Chavez, U. Even, and M. G. Raizen. Single-Photon Atomic Sorting: Isotope Separation with Maxwell's Demon. *arXiv*, 1001:0944v2 (2010).
- [20] U. Even, J. Jortner, D. Noy, and N. Lavie. Cooling of large molecules below 1K and He clusters formation. *J. Chem. Phys.*, **112** 8068 (2000).
- [21] J. A. Brand, J. E. Furst, T. J. Gay, and L. D. Schearer. Production of a high-density state-selected metastable neon beam. *Rev. Sci. Instrum.*, **63**, 163 (1991).
- [22] H. L. Bethlem, G. Berden, and G. Meijer. Decelerating Neutral Dipolar Molecules. *Phys. Rev. Lett.*, **83**, 1558 (1999).
- [23] S. Y. T. van de Meerakker, P. H. M. Smeets, N. Vandaecke, R. T. Jongma, and G. Meijer. Deceleration and Electrostatic Trapping of OH Radicals. *Phys. Rev. Lett.*, **94**, 023004 (2005).
- [24] B. C. Sawyer, *et al.* Magnetoelctrostatic Trapping of Ground State OH Molecules. *Phys. Rev. Lett.*, **98**, 253002 (2007).
- [25] H. L. Bethlem, G. Berden, A. J. A. van Roij, F. M. H. Crompvoets, and G. Meijer. Trapping Neutral Molecules in a Traveling Potential Well. *Phys. Rev. Lett.*, **84**, 5744 (2000).

- [26] G. Berden, R. Engeln, P. C. M. Christianen, J. C. Mann, and G. Meijer. Cavity-ring-down spectroscopy of the oxygen A band in magnetic fields up to 20 T. *Phys. Rev. A*, **58**, 3114 (1998).
- [27] W. G. Kaenders *et al.* Refractive components for magnetic atom optics. *Phys. Rev. A*, **54**, 5067 (1996).
- [28] E. Hecht. *Optics*. Addison-Wesley, 4th Ed. 2002.
- [29] S. Humphries. *Principles of Charged Particle Accelerators*. Wiley, New York, (1986).
- [30] J. C. Maxwell. *Theory of Heat*. Longmans, Green and Co., London (1875), 4th ed.
- [31] D. V. Schroeder. *An Introduction to Thermal Physics*. Addison Wesley Longman, New York (2000).
- [32] J. P. Sethna. *Entropy, Order Parameters, and Complexity*. Oxford University Press, (2006).
- [33] L. Szilard. On the decrease in entropy in a thermodynamic system by the intervention of intelligent beings. *Z. Physik*, **53**, 840 (1929).
- [34] L. Brillouin. Physical entropy and information. II. *J. Appl. Phys.*, **22**, 338 (1951).
- [35] C. E. Shannon. A mathematical theory of communication. *Bell System Tech. J.*, **27**, 379 (1948).

- [36] N. Vanhaecke, U. Meier, M. Andrist, B. H. Meier, and F. Merkt. Multistage Zeeman deceleration of hydrogen atoms. *Phys. Rev. A*, **75**, 031402 (2007).
- [37] S. D. Hogan, D. Sprecher, M. Andrist, N. Vanhaecke, and F. Merkt. Zeeman deceleration of H and D. *Phys. Rev. A*, **76**, 023412 (2007).
- [38] C. G. Parthey. *Pulsed Magnetic Slowing of Supersonic Beams*. University of Texas at Austin, Master Thesis (2007).
- [39] J. W. Beams and F. B. Haynes. The Separation of Isotopes by Centrifuging. *Phys. Rev.*, **50**, 491 (1936).
- [40] A. A. Artyukhov *et al.* Centrifuge enrichment of cadmium isotopes as the basis for further experiments on physics of weak interactions. *Nucl. Instr. and Meth. A*, **401** 281 (1997).
- [41] G. E. Popov, V. N. Prusakov, A. I. Rudnev, A. V. Tikhomirov, and A. V. Voronin. Centrifuge enrichment of chromium-50 for experiments on detecting solar neutrinos. *Nucl. Instr. and Meth. A*, **362** 532 (1995).
- [42] A. O. Nier. A Mass-Spectrographic Study of the Isotopes of Hg, Xe, Kr, Be, I, As, and Cs. *Phys. Rev.*, **52**, 933 (1937).
- [43] L. O. Love. Electromagnetic Separation of Isotopes at Oak Ridge: An informal account of history, techniques, and accomplishments. *Science*, **182**, 343 (1973).
- [44] P. A. Bokhan *et al.* *Laser Isotope Separation in Atomic Vapor*. WILEY-VCH Verlag Gmbh and Co. KGaA, Weinham, Germany (2006).

- [45] G. Bird. Direct Simulation Monte Carlo Method. http://sydney.edu.au/engineering/aeromech/dsmc_gab/.
- [46] J. P. Beardmore, A. J. Palmer, K. C. Kuiper, and R. T. Sang. A hexapole magnetic guide for neutral atomic beams. *Rev. Sci. Instrum.*, **80**, 073105 (2009).
- [47] K. C. Kuiper. *Magnetic bender for metastable neon lithography*. Eindhoven University of Technology, Master Thesis (2008).
- [48] V. N. Gorshkov, V. A. Komarovskii, A. L. Osherovich, and N. P. Penkin. Lifetimes of excited levels of Nd I and Nd II. Oscillator strengths of the spectral lines of Nd I. *Astrophysics*, **17**, 437 (1982).
- [49] W. A. van Wijngaarden and J. Li. Laser isotope separation of barium using an inhomogeneous magnetic field. *Phys. Rev. A*, **49**, 1158 (1994).
- [50] M. Jerkins, J. R. Klein, J. H. Majors, F. Robicheaux, and M. G. Raizen. Using cold atoms to measure neutrino mass. *New J. of Phys.*, **12**, 043022 (2010).
- [51] E. Narevicius, S. T. Bannerman, and M. G. Raizen. Single-Photon Molecular Cooling. *New J. of Phys.*, **11**, 055046 (2009).
- [52] I. Porra. Enhancement of neutron radiation dose by the addition of sulphur-33 atoms. *Phys. Med. Biol.*, **53**, L1 (2008).
- [53] D. Budker. *Atomic Physics*. Oxford University Press, 2nd Ed. (2008).

Vita

Isaac Chavez was born in El Paso, Texas on October 14, 1984 as the son of Gonzalo and Nora Chavez. He graduated from Riverside High School in El Paso, Texas in 2003. In 2007 he received his Bachelors of Science with honors from The University of Texas at Austin. Isaac began his graduate studies in the Fall of 2007 under the supervision of Mark G. Raizen at The University of Texas at Austin.

Permanent address: 8013 Algerita Ct.
El Paso, Texas 79915

This thesis was typeset with L^AT_EX[†] by the author.

[†]L^AT_EX is a document preparation system developed by Leslie Lamport as a special version of Donald Knuth's T_EX Program.